Friedrich-Alexander-Universität
Naturwissenschaftliche Fakultät

Bachelor Thesis
in Physics

Temperature stabilisation of an astrometric camera for the Medium-Sized Telescope for CTAO

Nils Nippe

Supervisor: Prof. Dr. Christopher van Eldik

Erlangen Centre for Astroparticle Physics

Submission date: 05.08.2025

Abstract

The Medium-Sized Telescope (MST) of the Cherenkov Telescope Array Observatory (CTAO) will be used to measure the Cherenkov light generated by cosmic gamma rays in the energy range of 150 GeV to 5 TeV in earths atmosphere. To archive the pointing criterium of < 7 arcsec, the MST will use a dedicated Pointing Camera (PCAM) for precise determination of its pointing direction and structure deformations. In previous work by Matzke, 2024, a temperature dependence of focal length, image rotation and pointing direction of the PCAM prototype was found and hypothesised to originate in the used lens. In this work, a temperature logging and regulation system using external instruments controlled by a Raspberry Pi 5 was developed. It archives a temperature stability of $T_{\mathrm{mean}} \pm \sigma_{\mathrm{T}} = (25.00 \pm 0.01)\,^{\circ}\mathrm{C}$ for a setpoint at least $10\,^{\circ}\mathrm{C}$ above the ambient temperature while staying within the power budget of the PCAM. The regulation is archived by resistive heating to the top of the operating temperature range of $25\,^{\circ}\mathrm{C}$. While the setup uses four PT100 temperature sensors at the time of writing, it is scalable to include up to ten sensors. The setup was tested in three campaigns pointing the PCAM at the sky in a constant position for one night each while recording the precise pointing direction using plate solving. This showed that the stabilisation of the lens temperature is insufficient to remove the temperature dependence of the pointing parameters of the PCAM. A correlation analysis between the measured temperatures and the pointing parameters was done during a sweep of the lens temperature, which suggests that the source of the focal length change is likely located in the vicinity of the camera temperature sensor (Spearman's rank correlation coefficient $r(T_{\mathrm{camera}}, f_{\mathrm{residual}}) = 0.98)$). No such clear correlation is found for the other pointing parameters. Further work is needed to accurately locate the source of the temperature dependence of the pointing parameters of the PCAM.

Contents

1 Introduction

1.1 Gamma ray Astronomy

When looking at the sky in energy ranges beyond those the visible light, many sources can be found. These sources exhibit a wide range of properties, including diverse output characteristics across various wavelength bands, distinctions between point-like and diffuse emissions and different light curves, with some exhibiting flares or bursts, while others have a very consist output profile.

Very High Energy (VHE) astronomy studies all wavelength bands above the extreme UV, including X-ray and gamma ray observations. In addition to electromagnetic messengers, neutrinos and Cosmic ray are also used.

When looking at high energy cosmic rays, there are three main distinct groups: gamma photons, electrons and heavier nuclei. Due to deflection in the interstellar magnetic fields, the latter two yield a mostly isotropic background (excluding close sources) and can't be used to image and differentiate astronomical sources (Kuhlen et al., 2023, Chap. 1). To find these cosmic accelerators, the gamma rays can be utilized, as their diffusion is a lot weaker than that of charged Cosmic ray (CR), even though their path is still slightly altered by their traversal of the Interstellar Medium (ISM).

After travelling through the Interstellar Medium (ISM), the cosmic rays arrive at the earth and interact with the dense (in relation to the ISM) medium for the first time after being produced. The earth's atmosphere places limitations on terrestrial high energy astronomical observations, as most particles get absorbed before they get to the ground. While the primary cosmic ray particle cannot be captured most of the time, the particle showers that get produced in the interactions with and within the upper atmosphere are measurable at ground level.

1.2 Air Showers

All Cosmic rays above a minimum energy have in common that they generate an Extensive Air Showers due to particle interactions with the atmosphere.Both gamma rays (GRs) and particle rays produces highly energetic secondary particles which produce tertiary particles themselves. This cycle repeats, resulting in a shower of particles until the minimum pair production energy cutoff is reached for the individual particles. As the particle number at the shower maximum $N_{\max}$ grows with increasing initial particle energy E_0 with $N_{\max} \propto E_0$, Extensive Air Showers are easier to detect at higher energies due to a higher Cherenkov light output (Stanev, 2010, Chap. 2). On the other hand, as the cosmic ray flux reaching earth follows a power law $F(E) = const \cdot E^{-\alpha}$ with $\alpha = 2.7$ below 3×10^6 GeV, more air showers are produced at lower energies (Stanev, 2010, Chap. 1).

1.3 Cherenkov Radiation

Most of the time, the secondary particles produced in an air shower are energetic enough that they travel faster than the speed of light in the medium, in this case the air in the upper atmosphere, which produces Cherenkov radiation. On a microscopic level, the moving particles polarize the medium, inducing oscillations in the medium atoms, which in turn radiate the introduced energy. If the particle velocity is larger than the

speed of light in the medium, the emitted radiation is coherent and can propagate in the far field instead of staying in the near field. The light gets radiated away from a particle travelling at a speed v (smaller than the speed of light in a vacuum c) through a medium with a refractive index n at an angle $\theta = \arccos\left(\frac{c}{vn}\right)$ relative to the particle direction (Kobzev, 2010). Typical angles in are are between 1.0° to 1.3° (Karle, 2006).

Extensive Air Showers are detected in four main ways (Konrad Bernlöhr, 2025):

- direct measurement of shower particles (Water-Cherenkov and scintillation detectors, Geiger-Müller counters)
- detection of produced radio waves
- atmospheric fluorescence light detection
- imaging of Cherenkov light

As each method has different advantages and drawbacks, detector projects focus on different scientific goals. While Imaging Air Cherenkov Telescopes (IACTs) mainly focus on lower energy ranges ($E_{\text{iact}} \lessapprox 10\,\text{TeV}$) with a small Field of View (FoV) ($\text{FOV}_{\text{iatc}} < 10\,\text{deg}$), Air Shower Arrays (ASAs) mostly detect showers with $E_{\text{asa}} > 10\,\text{TeV}$ with a large $\text{FOV}_{asa} > 45\,\text{deg}$ (HAWK, 2025). The ultra high energies are covered by radio detection systems focussing on an energy range above 100 PeV (Schröder, 2025, Chap. 3).

2 Imaging Air Cherenkov Telescopes

2.1 Current and Future Imaging Air Cherenkov Telescopes

At the moment, there are three main IACTs in operation: the High Energy Stereoscopic System (H.E.S.S.), the Major Atmospheric Gamma Imaging Cherenkov Telescopes (MAGIC) and the Very Energetic Radiation Imaging Telescope Array System (VERITAS). These all cover similar energy ranges for tens of GeV to tens of TeV with Major Atmospheric Gamma Imaging Cherenkov Telescopes (MAGIC) having a lower sensitivity than the other two (Knödlseder, 2016, Fig. 5; *HESS - The High Energy Stereoscopic System* 2021; *Welcome to VERITAS* 2004; *MAGIC performance* 2025). To enhance the sensitivity and broaden the optimized energy range towards upper and lower energy events, the Cherenkov Telescope Array Observatory (CTAO) is being developed and built at the moment. Cherenkov Telescope Array Observatory (CTAO) will cover a range from 20 GeV to 300 TeV (*Science with the Cherenkov Telescope Array* 2018).

2.2 Imaging Targets and Cherenkov Telescope Array Observatory Key Science Projects

The possible IACT imaging targets are well covered by the CTAO Key Science Project, defined by the CTAO Consortium alongside proposal-driven target selections. Science targets of IACT gamma ray observatories in general can be grouped into two main populations: galactic and extragalactic sources.

Extragalactic sources are mostly found in the lower energy ranges, as scattering and pair-production in interactions with the Extragalactic Background Light limits propagation of Ultra High Energy Gamma Rays (UHEGRs) over intergalactic distances.

For very distant sources, the observations are generally limited to the HE band ($<$ 100 GeV) (Prandini et al., 2022, Chap. 4).

Active Galactic Nucleis (AGNs) are galaxies that contain actively accreting Super-Massive Black Hole in their centre. Observations can probe accration physics, jet formation and feedback into the host galaxy. The AGN Key Science Project will observe a representative subset of very high energy AGNs and take time-resolved spectra and light curves, both in a normal semi-quiescent state and as a response to AGN flare alerts. (*Science with the Cherenkov Telescope Array* 2018, Chap. 12)

A blind survey of 25% of the sky in the 50 GeV to 10 TeV energy range will provide an unbiased Very High Energy (VHE) map, including potential new gamma ray sources, Starburst Galaxies and Galaxy Clusters. (*Science with the Cherenkov Telescope Array* 2018, Chap. 8)

The Milky Way will be covered by both a general Galactic Plane Survey and a deeper exposure of the galactic centre. The Galactic Plane Survey will map the entire galactic plane with an emphasis on promising regions (e.g. within the central $\pm 60°$). These surveys are intended to provide an extended galactic source catalogue allowing the identification of follow-up targets, measure the diffuse emission within the galactic plane and discover new high energy phenomena. (*Science with the Cherenkov Telescope Array* 2018, Chap. 6) The Galactic Centre Survey will consist of deep exposures of the central 1.5°, including Sgr A*, various Pulsar Wind Nebulae and Supernova Remnants (*Science with the Cherenkov Telescope Array* 2018, Chap. 5). The identified sources in both the Galactic Plane Survey and Galactic Centre Survey (GCS) are expected to be mostly Supernova Remnants, Pulsar Wind Nebulae and gamma ray binaries, with Pulsar Wind Nebulae being the most abundant.

In addition to gamma ray observations, Imaging Air Cherenkov Telescopes (IACTs) can also detect air showers created by charged Cosmic rays by the same Cherenkov mechanism. This will provide data about the nucleic composition and electron component of Cosmic rays. (*Science with the Cherenkov Telescope Array* 2018, Chap. 14)

2.3 Cherenkov Telescope Array Observatory

In the alpha configuration, the CTAO will be made up of 64 telescopes of three different sizes, all optimized for different Cosmic ray energies, spread over the North and South sites.

While the total expected signal of Extensive Air Showerss (EASs) is comparably small relative to other signal sources like stars, its unique time signature on the scale of nanoseconds makes it possible to detect them above these background signals (Holder, 2015, Chap. 2). As the photon density is still small, on the order of 100 photons/m^2 for 500 GeV showers, sensitive readout electronics and clean signal amplification (often implemented with Photo Multiplier Tubes (PMTs)) are needed, to enable a detection of individual photons (Holder, 2015, Fig. 4 and Chap. 4.3).

The hillas parameters of the fit ellipse (shown in the bottom Figure 1) together with the telescope pointing data are used to reconstruct the shower impact point from an image of a single telescope. Using multiple separated telescope to image the same EAS improves this reconstruction by constructing a convergence point of the different imaged shower axes, directly producing the shower direction and impact point, as shown in Figure 1.

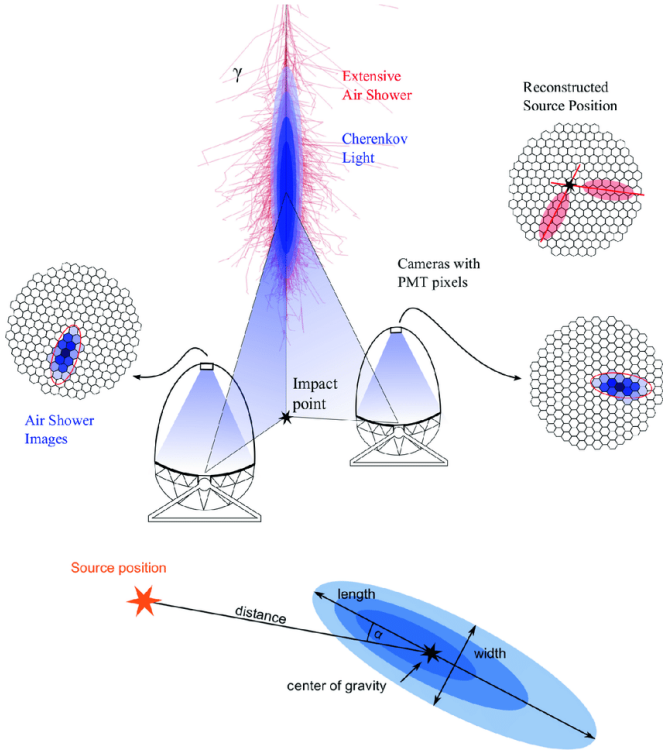

Figure 1: Gamma ray direction reconstruction using multiple Imaging Air Cherenkov Telescope (from Bose et al., 2022, Figure 4, originally by the MAGIC Collaboration).

The expected sensitivity of CTAO at shorter observation times (50 h in Figure 2) is greater than any currently existing gamma ray telescope. For a rough comparison, Cosmic Ray Simulations for Kascade (CORSIKA) simulations were done for CTAO to get the sensitivity curves, though these comparisons are to be approached with caution, as there are different energy bins and detection criteria for each telescope. For CTAO, this corresponds to the lowest flux at which a point-like source can be detected with a statistical significance of 5 standard deviations (Observatory and Consortium, 2021, Sensitivity). In the lower energy range below 100 GeV, Fermi Large Area Telescope (Fermi-LAT) has enhanced sensitivity for long-term observation (and, as such, for non-transient phenomena), as the differential flux sensitivity flattens out at around the one week mark, as shown in Figure 3. For gamma ray energies above 10 TeV, the Large High Altitude Air Shower Observatory and the Southern Wide-field Gamma-ray Observatory get higher sensitivities after one and five years, respectively. With its increased sensitivity, CTAO aims to increase the number of known astronomical gamma ray sources by a factor of five to ten (*Technical specifications - CTAO* 2025).

The CTAO is split into a north and south site which are instrumented somewhat differently as to tailor the respective capabilities to the specific site targets. The northern array on La Palma will focus on galactic gamma ray sources and is optimized for an energy range of 20 GeV to 5 TeV, which covers these sources. It is being built on the same site as the MAGIC observatory and will host four Large-Sized Telescopes (LSTs) and nine Medium-Sized Telescopes (MSTs) (*CTAO North - CTAO* 2025). From the southern site near Paranal in the Atacama Desert, the galactic centre and a large portion

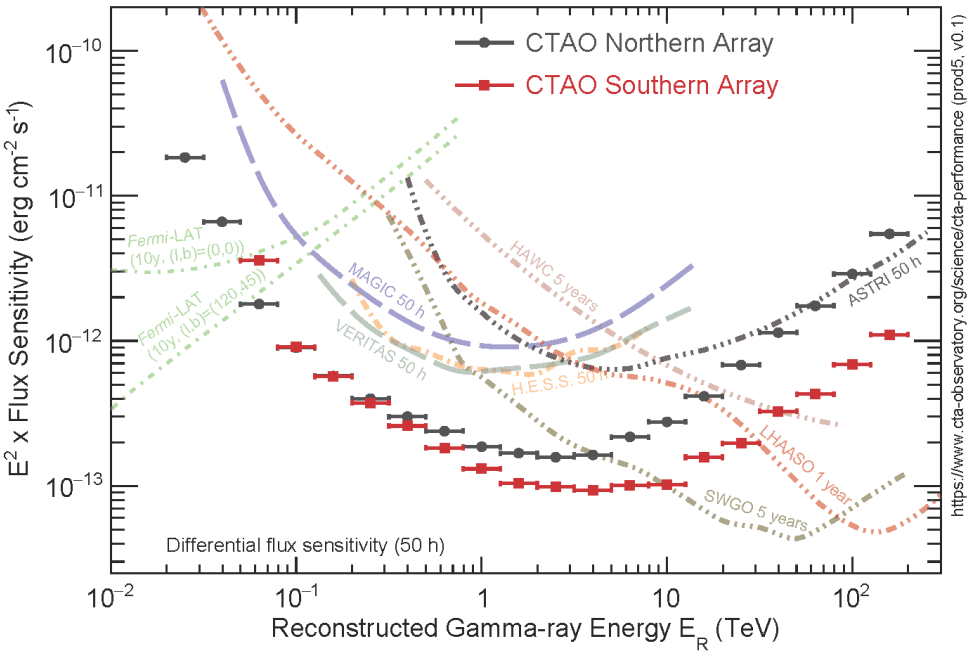

Figure 2: Differential sensitivity of CTAO to make a 5σ detection of a point-source compared to other instruments (from (Observatory and Consortium, 2021, Sensitivity))

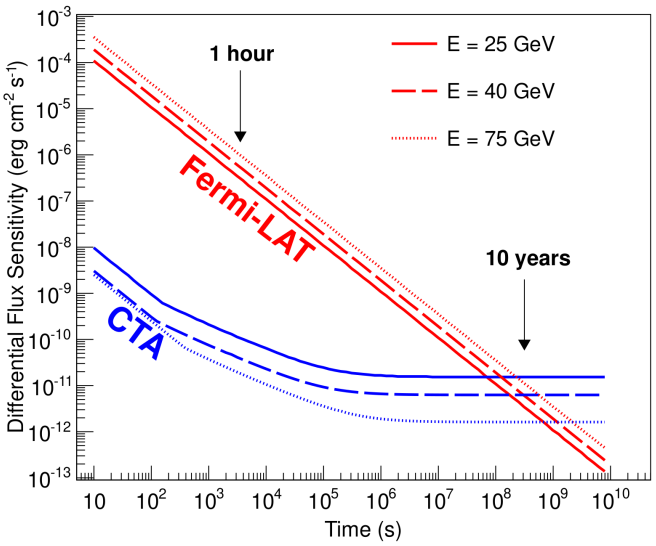

Figure 3: Differential sensitivity of CTAO to make a 5σ detection of a point-source for different lower energies compared to Fermi-LAT (from (*Science with the Cherenkov Telescope Array* 2018, Figure 1.4))

of the Milky Way is visible, hence the optimization for the expected higher energies from 150 GeV to 300 TeV. While the planned Alpha configuration of CTAO includes 14 MSTs and 37 Small-Sized Telescopes (SSTs), foundations for a possible future upgrade with four LSTs and an additional three SSTs are included.

As CTAO North is close to the Paranal Observatory site, the climate data from its weather station can be used to estimate the expected operating envelope of the new telescopes. Compared to the 0.5% and 99.95% percentiles between 1. Jan 2000 and 31. Dec 2022 of 1.6 °C and 21.0 °C, the quoted operating temperature range of −5 °C to 25 °C covers the extremes well (*ESO - Astro Climatology* 2025; Specovius, 2022). These temperature ranges need to be taken into account for all CTAO subsystems that are designed to be exposed to the outside, like the PCAM.

Low energy air showers are more frequent, as the gamma ray spectrum falls of towards higher energies, but provide less overall Cherenkov light (see subsection 1.2). This requires more light-sensitivity for a detection, which explains the inverse relation between the optimized energy range and the telescope size in CTAO. The smaller telescopes can in turn be spread out, instrumenting a larger area, which is needed to get enough detections of higher energy particles at their lower flux during observations. Subsequently, three different telescope sizes are needed to efficiently image the large energy range planned for CTAO, as there are different signal timescales and powers to be expected when looking at air showers with different initial particle energies.

A comparison of the relevant characteristics of the individual telescopes is listed in Table 1.

	SST	MST	LST
Energy range	5 TeV − 300 TeV	150 GeV − 5 TeV	20 GeV − 150 GeV
Effective mirror area	$> 5\,\mathrm{m}^2$	$88\,\mathrm{m}^2$	$370\,\mathrm{m}^2$
(number of telescopes)	(South: 37)	(N: 9, S: 14)	(North: 4)
Pointing precision	$< 7''$	$< 7''$	$< 14''$
Mirror diameter D	4.3 m	11.5 m	23.0 m
Focal length f	2.15 m	16 m	28 m
f-Number (f/D)	$f/0.5$	$f/1.39$	$f/1.22$
Slewing time	70 s	90 s	30 s

Table 1: Characteristics of the different telescope types in CTAO (*Technical specifications - CTAO* 2025)

In addition to whole-array operation, the telescopes can be grouped into sub-arrays, which can be used for different observations simultaneously. This increases flexibility when looking at multiple variable sources or source types which do not require the whole energy range capabilities of the CTAO. A split array can also image a larger FoV, which allows a follow-up observation for an alert with a larger uncertainty on the initial pointing position, as can be the case in a gravitational wave observation. (*Science with the Cherenkov Telescope Array* 2018, Chap. 1.1)

The fast slewing times (see Table 1) allows the CTAO array to ingest alerts from other observatories and can respond to newly discovered transient phenomena to observe, for example, the immediate afterglow of a gamma ray burst or play a part in multi-messenger observations of transients with neutrino or gravitational wave observatories.

As well as ingesting alerts, an automatic data analysis pipeline allows the automatic issuing of alerts of gamma ray activity to other instruments within one minute after the initial detection.

As this work is concerned with a subsystem of the MST, the two other telescope types are not further discussed.

2.4 Medium-Sized Telescope

The MST is built as a modified Davies-Cotton design, both providing an adequate Point Spread Function (PSF) (PSF $\sigma_{80} < 0.18$ for all angles $< 2.8°$ from the FoV centre) and distorting the photon arrival time from different mirror facets as little as possible (rms optical time spread < 0.8 ns over 80% of the FoV). The PSF was optimized so that 80% of the intensity from a point source at infinity gets projected into a circle of about the same size of single pixel of the FlashCam. The small time distortion is needed to efficiently and accurately reconstruct the shower direction from the photon arrival times. The main mirror is made up of 86 hexagonal mirror segments, which are mounted to a steel backstructure via a set of actuators to allow for mirror alignment during commissioning and when mirror recoating or replacement becomes necessary (Garczarczyk, 2022, Chap. 4).

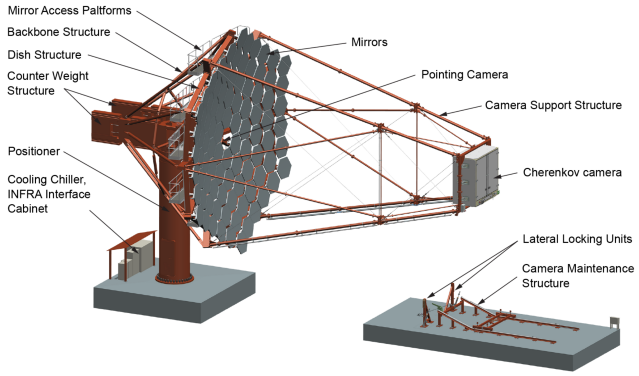

Figure 4: MST Overview (from Garczarczyk, 2022, Fig. 1.2)

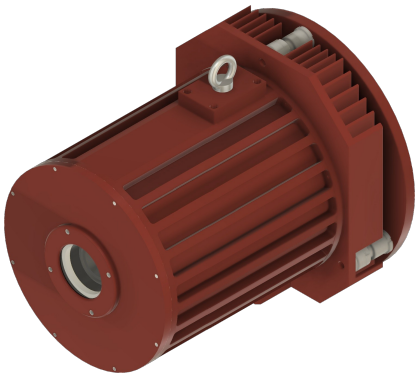

Figure 5: PCAM outside view (from Schaefer, 2025)

2.4.1 Pointing Strategy

For the MST, there are three sources of deviations from the commanded pointing directions (Ullrich Schwanke, 2022, Chap. 4):

a) angular offsets and non-linearities in the azimuth and elevation drive encoders

b) misalignments between azimuth and altitude axes

c) reproducible and non-reproducible deformations of the telescopes structure

Reproducible structure deformations are caused by sagging and torsion forces acting in different directions dependent on where the telescope is pointing. These can be calculated by using precomputed structure model which takes the pointing direction as an input. Non-reproducible deformations are caused, for example, by wind forces

acting on the telescope, which need to either be corrected during observations or taken into account when doing data analysis afterwards.

As such, the corrections applied onto the telescope pointing are also split into *standard astrometric corrections* and *precision astrometric corrections*, the first correcting for reproducible, slowly changing (timescale on the order of weeks to months), deformations of the telescope pointing geometry. The latter will need to be determined concurrent to gamma observations, as these cannot be pre-calculated.

As the deviations are expected to be small compared to the telescope FoV, no active tracking will be needed and all corrections can be applied to the data afterwards. Both correction types taken together, the MST pointing criteria are required to be below 7 arcseconds by the CTAO Consortium.

The precise pointing strategy can be further split into two pipelines: one will find the telescope pointing direction by plate solving and the other will calculate the deformations of the structure by measuring the precise position of the FlashCam (FlashCam) relative to the telescope mirror. First, a spot extraction is done on the PCAM output image to find both the position of stars in the image as well as the LEDs positioned in a ring around the FlashCam. The star positions are then fed into a plate solver, which hashes the extracted triangular or quad structures to known structures from a star catalogue. The LED positions are similarly fitted and both position datasets are fed into the pointing model fitter, which outputs the needed corrections. An overview of the whole process can be found in Figure 6.

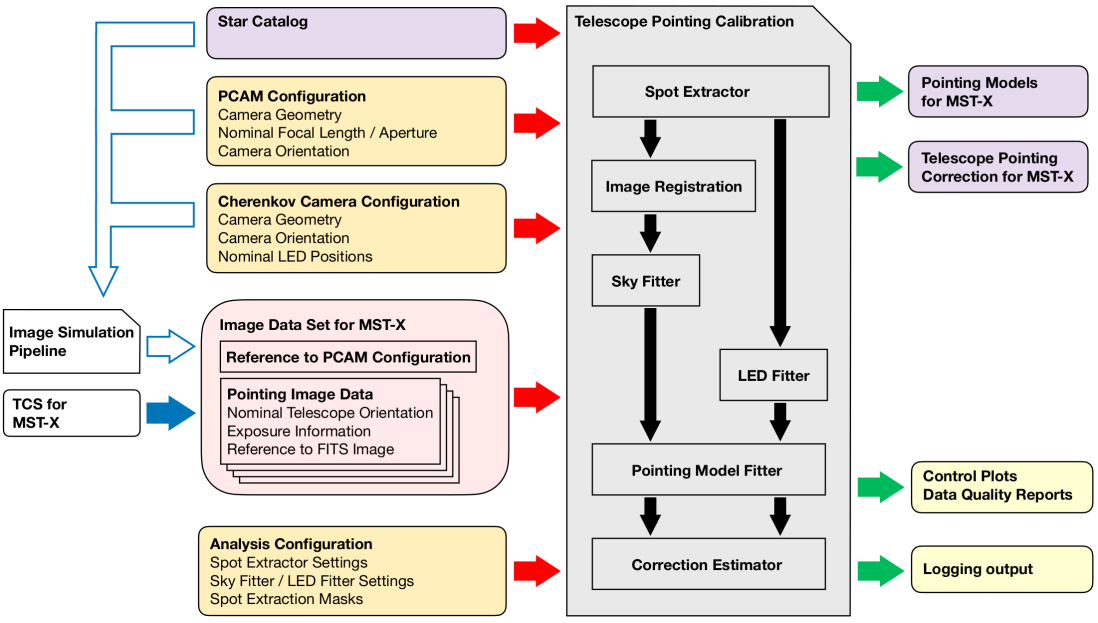

Figure 6: Pointing calibration strategy flowchart (from Schwanke, 2022, Figure 4.1)

2.4.2 Medium-Sized Telescope Pointing Camera

The pointing camera is mounted in the centre of the main mirror of the MST and is pointed towards the Cherenkov camera. It is mainly made up of a modified ZWO ASI2600-MM Pro CMOS camera, a Nikon AF NIKKOR 50mm 1:1.8 D lens and a

Advantech MIO-2361EW-S1A2 (Atom E3930) industrial mini-computer. The computer controls the camera, reads environmental sensors (humidity and temperature) sensors placed within the PCAM enclosure and interfaces with the telescope network over ethernet. An aluminium housing with a heated viewport is enclosing the entire setup to protect the sensitive electronics from environmental effects. The CMOS camera has been modified by removing its housing and cooling ribs in the back to instead couple it to the PCAM housing with a copper head conductor. (Specovius, 2022)

The internal construction is shown in Figure 7 and Figure 8.

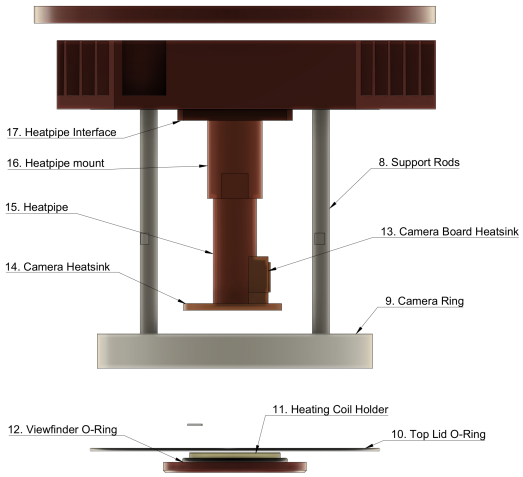

Figure 7: Overview of PCAM internal components (from Schaefer, 2025)

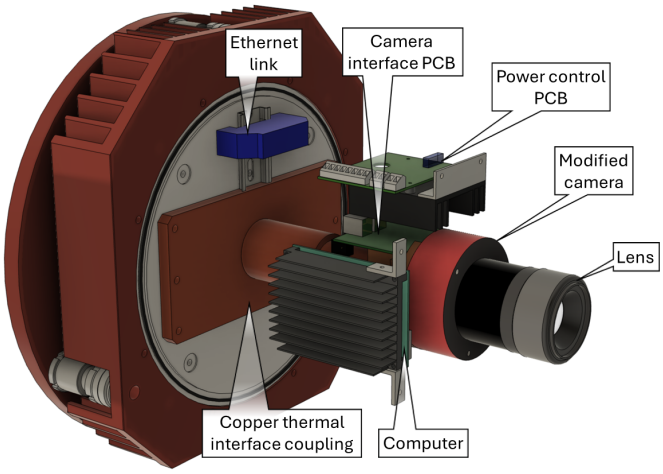

Figure 8: Internal components including the camera and lens (from Matzke, 2024, Fig. 6)

The PCAM can image a FoV of around $26.5° \times 17.8°$, encompassing the LED-ring around the main camera and the starfield behind it (Specovius, 2022). The camera is focussed such that the LED ring lies at half the hyperfocal distance, which produces equally blurred projections of the LEDs at about 16 m and the stars at infinity. Feeding these images through the image processing pipeline described in Figure 6, a precise pointing direction is returned.

3 Temperature dependant pointing deviations of PCAM prototype

In Matzke, 2024, the LEDs for the relative positioning between PCAM and the MST-Camera (MSTCam) were developed and characterized. During this work, the PCAM was mounted onto a *Rainbow Astro RST-3000* goto mount on a *Berlebach Planet lang* tripod and placed inside a lab room.

The PCAM was placed in front of a ring of LEDs at a distance of around 16 m and focused to the hyperfocal distance of 32 m. This simulates the final setup in the MST. As this was before the temperature sensors were placed on the lens and in the housing, the only measured temperatures were directly at the camera chip and inside the housing with an additional environmental sensor. During all measurements in the lab, this setup was reproduced.

To test the pointing stability, images are taken of this ring of LEDs and a position fit is done for the 12 LED positions, which then get combined into a final camera pointing position. During tests to optimize the chip cooling temperature setpoint, a temperature dependence of the pointing position was found by sweeping the setpoint to a range of values between −10 °C and 15 °C. An attempt was made to calibrate this temperature dependence with a 2nd order polynomial fit, which at first seemed to be successful. The results of this fit are shown in Figure 9. As the camera rotation within the housing was changed after this measurement, the mapping of the x and y offset and the real word directions have changed.

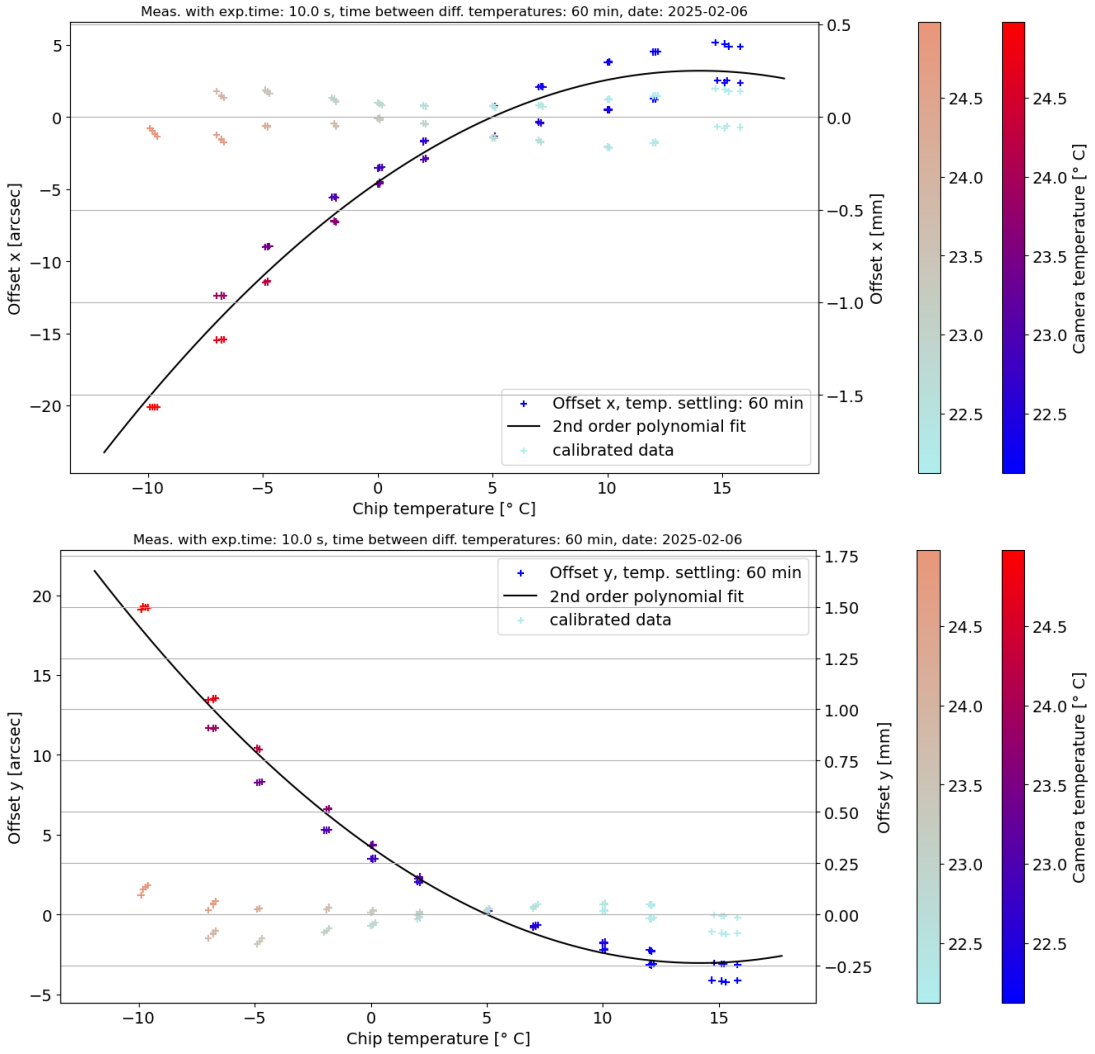

Figure 9: Pointing position dependency on PCAM chip temperature from Matzke, 2025.

To follow up and further quantify this temperature dependence, tests were done heating the entire PCAM housing. To isolate two potentially distinct effects, this test was done without any chip cooling. The whole PCAM was wrapped with a temperature regulated heating mantle, insulated with aluminum foil and heated to around 35 °C, 40 °C and 45 °C and then left to cool down. It is to be noted, however, that the temperature steps were not done with sufficient time between steps, thus no steady

state was able to develop and the chip temperature was still rising towards the setpoint when the next step was started. This resulted in the plots shown in Figure 10 and Figure 11. The Science Cam focal length and the PCAM focal length can be converted between each other by

$$\frac{f_{\text{lens, solved}}}{f_{\text{lens, nominal}}} = \frac{f_{\text{science cam, nominal}}}{f_{\text{science cam, solved}}} \tag{1}$$

using $f_{\text{lens, nominal}} = 50\,\text{mm}$ and $f_{\text{science cam, nominal}} = 16\,\text{m}$. The Science Cam focal length is equivalent to the distance between the PCAM and the ring of LEDs. All values with the prefix *residual* are calculated by subtracting the mean value of the entire dataset from the respective values.

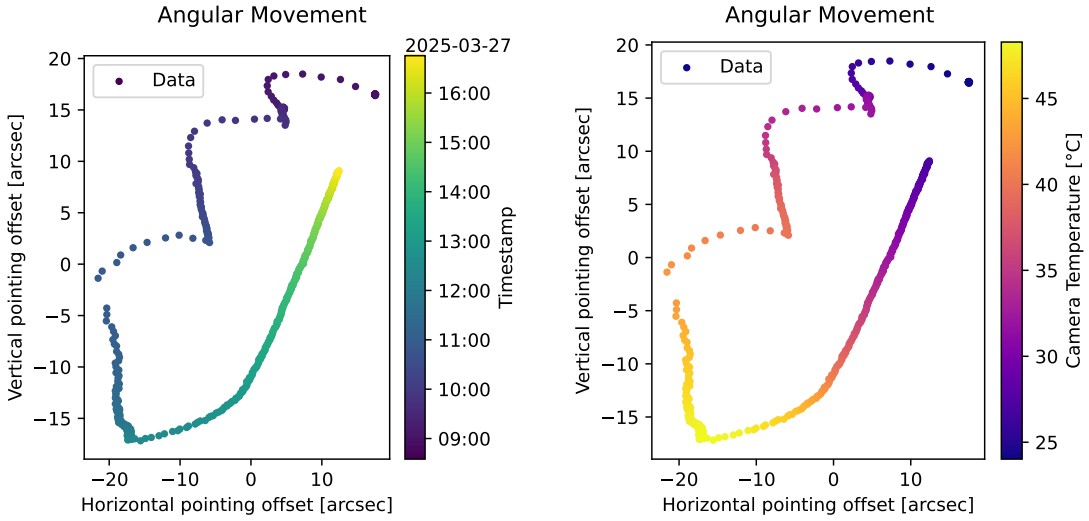

Figure 10: Angular movement of Pointing Camera (PCAM) pointing direction when heating the camera housing from the outside in three steps (Data from Matzke, 2025).

In both plots a strong hysteresis can be observed, which drastically complicates any attempts at calibrating a temperature dependency, which would now need knowledge of the temperature history of the PCAM. While the hysteresis for the rotation and the focal length is not as strong as for the pointing direction, the difference is still enough to exceed the targeted precision.

The hysteresis combined with the lack of a steady state makes a truly meaningful plot impossible, as the data cannot be filtered to a settled state. Still, to have any chance of comparing the previous heating campaign to the new lens temperature sweep in section 6, a fit of the temperature dependency of the residual focal length and the residual rotation was performed. As the system shows different behaviors for rising (↑) and falling (↓) temperature, the dataset was split into two branches at time with the highest temperature. To enable a fit to converge, the mean of every 10 datapoints was taken. As the later fits were all done with a linear relation $f(x) = a \cdot x + b$, this model was also used here, which gets an ok fit for the focal length and rotation and the branch of falling temperature in general. For the rising branch the fit does not agree with the data very well due to the large hysteresis and the lack of possible filtering to a steady state.

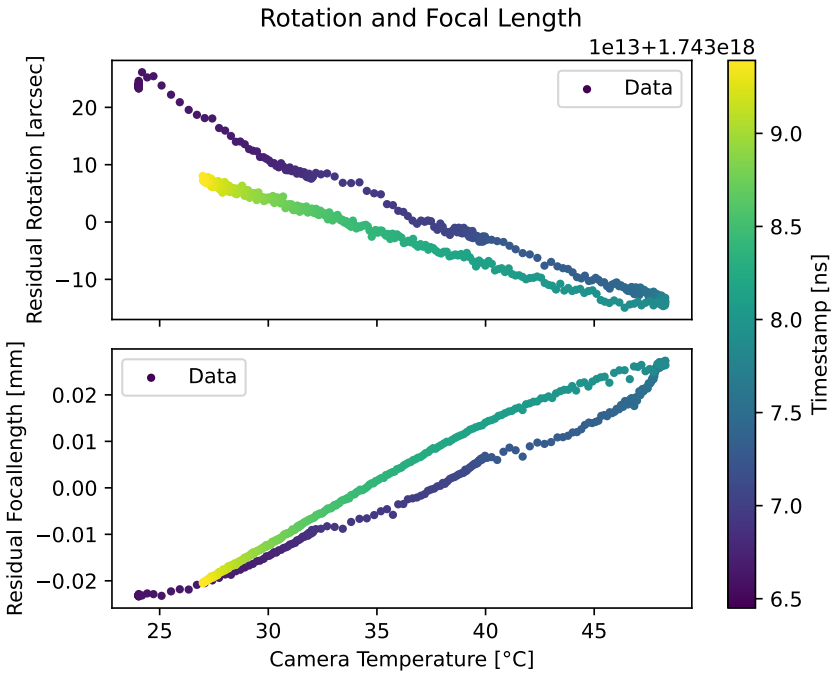

Figure 11: Focal length and rotation of Pointing Camera (PCAM) when heating the camera housing from the outside in three steps (Data from Matzke, 2025).

The resulting fit for the residual focal length and residual rotation is shown in Figure 12 and the fit for the angular movements is shown in Figure 36 in the appendix. The parameters for the fits are listed in Table 2.

Fit value	Branch	Fit parameters ± fit uncertainty
Residual focal length	↑	$a = (201.7 \pm 2.5) \times 10^{-5}\,\mathrm{mm\,K^{-1}}$
		$b = (-71.3 \pm 0.8) \times 10^{-3}\,\mathrm{mm}$
	↓	$a = (256 \pm 5) \times 10^{-5}\,\mathrm{mm\,K^{-1}}$
		$b = (-89.1 \pm 1.3) \times 10^{-3}\,\mathrm{mm}$
Residual rotation	↑	$a = (-1.541 \pm 0.027)\,\mathrm{arcsec/K}$
		$b = (60.0 \pm 1.1)\,\mathrm{arcsec}$
	↓	$a = (-1.099 \pm 0.013)\,\mathrm{arcsec/K}$
		$b = (37.0 \pm 0.4)\,\mathrm{arcsec}$

Table 2: Fit parameters of fit results shown in Figure 12 (Heating Campaign).

Based on these observations, it was assumed that some thermal expansion within the lens is cause for the temperature dependence. This work therefore is concerned with the temperature stabilization of this part of the PCAM.

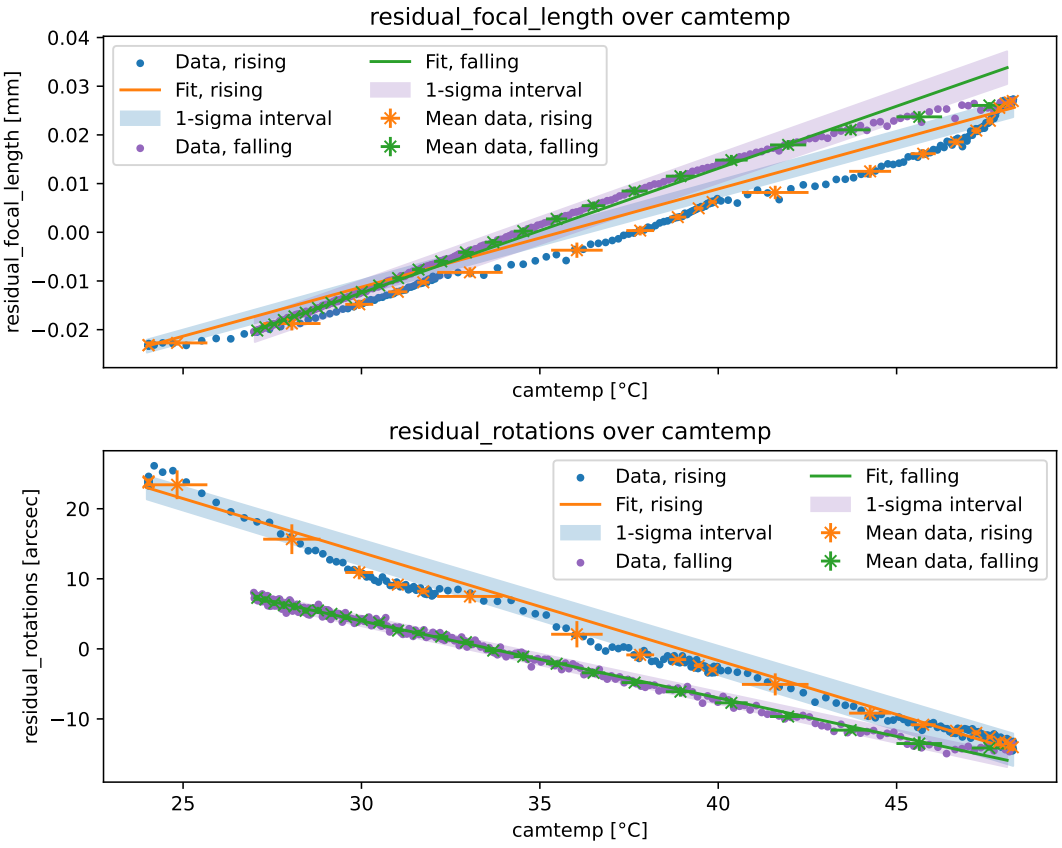

Figure 12: Fit of residual focal length and rotation of Pointing Camera (PCAM) when heating the camera housing from the outside in three steps (Data from Matzke, 2025).

4 Heating setup

The input power provided to the PCAM is set at $(12.0 \pm 0.5)\,\mathrm{V}$ and a maximum power of 96 W (Steiner, 2022, Chap. 3.3.1). To reserve some power for the PC and camera, the available heating power was set to 60 W. This places limits on the overall heating energy available as well as constraining what thermal control setups can be used.

As the upper limit of the operating temperature range of 25 °C is within reasonable working limits of all PCAM components, temperature regulation can be achieved purely by heating to the upper limit. This simplifies the electronic design, as it only requires a single-quadrant power supply and controller instead of a dual-quadrant supply needed for controlling a peltier element.

To distribute the heating around the lens, a ring of resistors in series was fabricated and taped to the camera ring (see part 9 in Figure 7 and Figure 13).

To get a maximal power output, resistor values of

$$R_{\mathrm{i,\ optimal}} = \frac{U_{\mathrm{max}}^2}{n_{\mathrm{resistors}} P_{\mathrm{max}}} = \frac{((12.0 \pm 0.5)\,\mathrm{V})^2}{6 \cdot 60\,\mathrm{W}} = 0.4\,\Omega \tag{2}$$

would be optimal. Due to better availability, Vitrohm power wirewound resistors type *KH210-8* with a value of $0.68\,\Omega \pm 10\%$ and an individual power limit of 7 W were chosen (*Power Wirewound Ceramic Resistors, axial* 2008). The resistance of the entire ring was measured to be $4.32\,\Omega$. This limits the heating power to

$$P_{\mathrm{max}} = \frac{U_{\mathrm{max}}^2}{n_{\mathrm{resistors}} R_i} = \frac{((12.0 \pm 0.5)\,\mathrm{V})^2}{6 \cdot 0.68\,\Omega} = (35 \pm 5)\,\mathrm{W} \tag{3}$$

which is already close to the power limit of $P_{\mathrm{max,\ series}} = n \cdot P_{\mathrm{max,\ individial}} = 42\,\mathrm{W}$. Measurements confirmed the maximum drawn power at 12 V to be 33.07 W.

A PT100 temperature sensor was attached to the outside of the lens body to monitor the lens temperature. The PT100 is a thin film platinum resistance thermometer, which increases its resistance R with rising temperature T according to

$$R(T) = R(0\,^\circ\mathrm{C}) \cdot (1 + A \cdot T + B \cdot T^2) \tag{4}$$

with coefficients $A = 3.908\,02 \times 10^{-3}\,^\circ\mathrm{C}^{-1}$ and $B = -5.802 \times 10^{-7}\,^\circ\mathrm{C}^{-2}$, which can be converted back to a temperature using

$$T = \frac{-AR_0 + \sqrt{(AR_0)^2 - 4BR_0(R_0 - R)}}{2BR_0} \tag{5}$$

within a temperature range of 0 °C to 850 °C (*DIN EN IEC 60751:2023-06* 2023). For the temperature range below 0 °C, an additional term $C \cdot (T - 100\,^\circ\mathrm{C}) \cdot T^3$ with $C = -4.2735 \times 10^{-12}\,^\circ\mathrm{C}^{-3}$ is added. The used sensor has a Class A accuracy, which corresponds to a systematic uncertainty of $\sigma_{\mathrm{sys}} = \pm(0.15 + 0.002|T|)^\circ\mathrm{C}$, which results in $\sigma_{\mathrm{sys,\ max}} = \pm 0.24\,^\circ\mathrm{C}$ in the temperature range used in this work (*PT100 Datasheet* 2022; *DIN EN IEC 60751:2023-06* 2023).

The resistance of the PT100 sensor was recorded using a 4-wire measurement and converted to a temperature reading with a *Keithley DMM6500* 6 1/2 Digit Multimeter. A 4-wire resistance measurement uses two wires to supply a constant measurement current to the sample under test and uses two additional wires connected to the sample

at the same points to measure the voltage drop over between the test points. In a 2-wire measurement, the the resistance of the current supply cables creates a systematic uncertainty on the recorded sample resistance. The DMM6500 has an accuracy of $\pm 0.80\,°\mathrm{C}$ and $\pm 0.06\,°\mathrm{C}$ when measuring resistance thermometers in 2-wire and 4-wire mode respectively. As we are mostly concerned with the stability of the temperatures and not necessarily with the absolute temperature values, all following given values only the statistical uncertainty.

An AIM-TTI QL564TP power supply was used to provide the heating power.

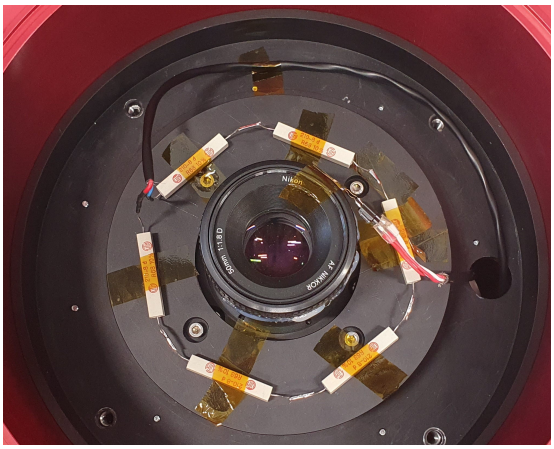

Figure 13: Initial resistor placement on camera ring, with the 4-wire temperature sensor visible at the top right of the lens.

4.1 Heating tests without and with partial insulation

To test the required heating power, a setup entirely without further insulation was tested at the maximum available heating power at 12 V. This resulted in a steady-state temperature of $(41.07 \pm 0.21)\,°\mathrm{C}$ at a room temperature of around 23 °C. Even with the naive approximation that the heat loss is linear with the surrounding temperature, the maximum heating power would thus not be sufficient to reach an internal temperature of 25 °C at the lower limit of the operating range. To lower the required heating power, foam insulation was added in a ring surrounding the lens, as can be seen in Figure 16.

Basotect G+ foam was used as insulation material due to a low thermal conductivity between $29\,\mathrm{mW\,m^{-1}\,K^{-1}}$ and $35\,\mathrm{mW\,m^{-1}\,K^{-1}}$ for −10 °C and 25 °C, respectively (*Basotect G+* 2011) and good mechanical properties. In addition, as this foam is normally used for sound insulation, it has good long-term stability, is flame-retardant and has excellent availability. As a mounting option with the heating resistors directly on top of the foam was considered at the beginning, a resistor taped onto a foam block and heated with a 12 V power supply, which resulted in no melting or degradation to the foam.

To avoid condensation inside the PCAM housing when running tests below ambient temperature, silica gel beads were placed in the lower housing area.

This setup was then placed in an *Espec ARG-1100* climate chamber and initially tested at 10 °C, 0 °C and −10 °C at different heating power levels, resulting in the temperature trace shown in Figure 14. The different exponential decays towards the

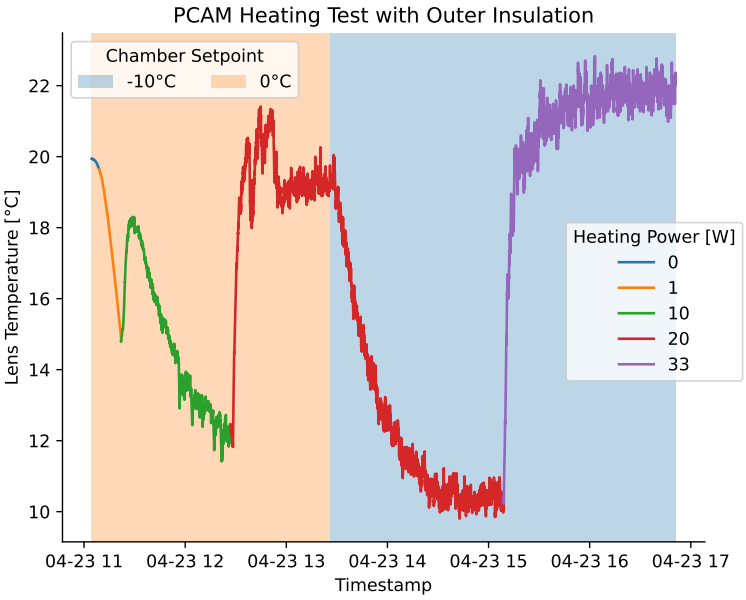

Figure 14: Temperature trace of lens sensor during heating test with ring insulation setup as seen in Figure 16 at different heating power levels and climate chamber temperature setpoints.

steady state were fitted and resulted in the following steady state temperatures measured at the lens:

Chamber setpoint [°C]	Heating power [W]	Steady state lens temperature ± fit uncertainty [°C]
10	33	41.042 ± 0.024
0	10	10.905 ± 0.024
0	20	19.257 ± 0.006
-10	20	10.191 ± 0.006
-10	33	$21.9164 \pm 0.0.0028$

Table 3: Steady state lens temperatures at different surrounding temperatures and heating levels using the ring insulation setup.

This test showed that either a higher heating power or better insulation would be necessary to reach a stable 25 °C lens temperature. As a higher efficiency is desirable to conserve power for other PCAM components, two new foam parts were added to the insulation to cover the top and bottom plates around the lens.

4.2 Heating test with insulation

The camera ring (see part 9 in Figure 7) and the top lid were identified as the largest remaining heatsinks with the ring insulation. These parts were insulated with two additional foam pieces, which can be seen in Figure 17. As the resistors were previously

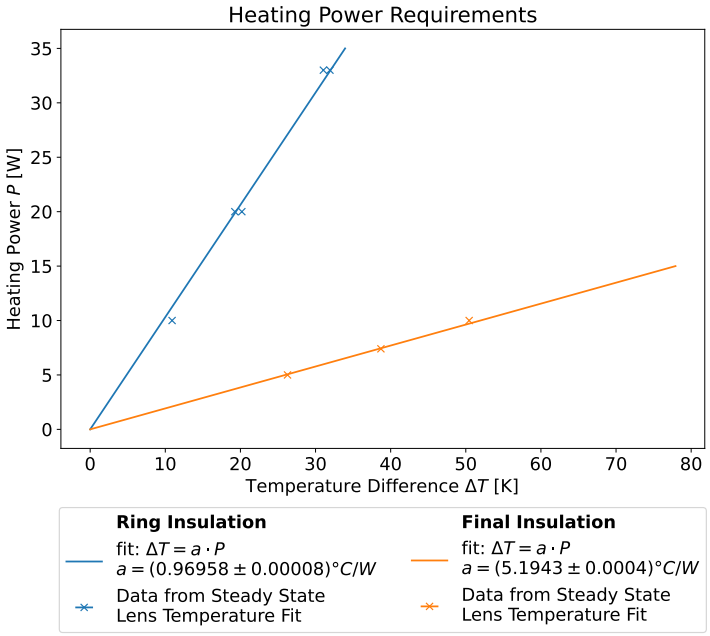

Figure 15: Heating power requirements of ring insulation with data from steady state fits from Figure 14 (respectively Table 3).

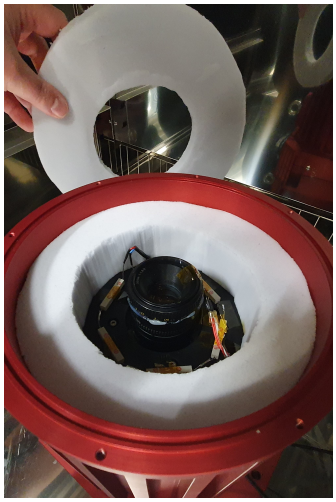

Figure 16: Initial resistor insulation setup (referred to as *ring insulation*), with upper ring to be placed on top of lower ring.

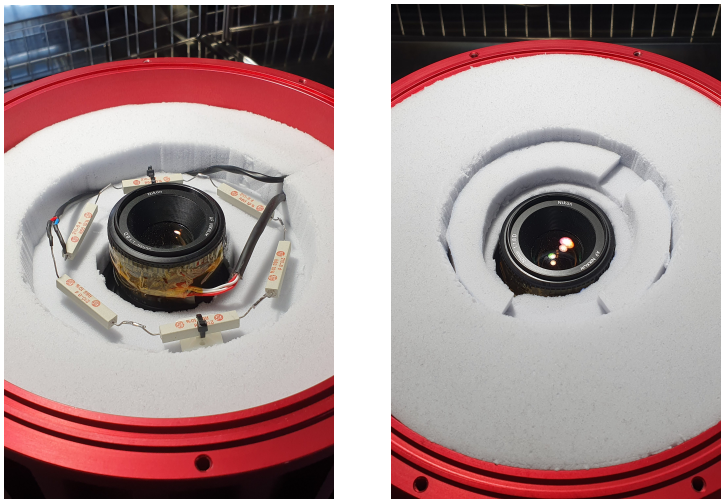

Figure 17: Final resistor insulation setup with resistor mounting (left) and complete inner insulation (right). The cutouts in the inner ring are needed to accommodate for the window heating parts.

placed directly onto the camera ring, they were moved on top of the lower foam piece and mounted using zip-ties and cable tie mounts.

An exploratory test was done at $-10\,^{\circ}\mathrm{C}$ external temperature and a heating power of 33 W, which resulted in a joint between two resistors desoldering itself after 3 minutes. This clearly showed the need for an active heating power controller, which is described is section 5.

After repairing the broken joint, two more cautious tests were carried out at lower heating levels, resulting in the following steady state lens temperatures:

Chamber setpoint [°C]	Heating power [W]	Steady state lens temperature ± fit uncertainty [°C]
0	5	26.27 ± 0.04
-10	7.4	28.7019 ± 0.0029
-10	10	40.448 ± 0.008

Table 4: Steady state lens temperatures at different surrounding temperatures and heating levels using the final insulation setup.

Both insulations showed a linear relationship between the difference of the lens and external temperatures and the required heating power to reach this difference. This relation was fitted with a linear equation without an offset, as a non-zero steady state temperature difference without any input power would be nonphysical. The resulting plot is show in Figure 15 and clearly shows the higher efficiency of the final insulation setup, which only requires $P_{\mathrm{heating}}(\Delta T = 35\,^{\circ}\mathrm{C}) = (6.7382 \pm 0.0006)\,\mathrm{W}$ instead of the $P_{\mathrm{heating}}(\Delta T = 35\,^{\circ}\mathrm{C}) = (36.0981 \pm 0.0030)\,\mathrm{W}$ for the ring insulation.

5 Heating Regulation

5.1 Temperature Sensor Placement and Readout

To measure the response of a larger area of the PCAM, more temperature sensors were needed. In addition to directly on the lens housing, these were placed between the inner side of the housing and the insulation, hanging free inside the bottom housing compartment and outside of the housing with a few centimeters distance to the top lid. All the individual sensor positions are shown in Figure 19.

The sensor between the housing and the insulation was mainly used to monitor if the housing had reached the climate chamber setpoint during cooled tests. The external sensor was used to measure the air temperature, which is why it was placed with some distance to the housing. As it was not connected to any thermal mass, its measurements were following small thermal fluctuations rapidly and were influenced by turbulences and windchill. To monitor the heat conducting to the back of the PCAM and to measure the influence of the heat output of the computer and astrocam, the last sensor was placed in the back compartment with some distance to all surrounding structures.

Due to the larger number of measurement points, a sensor redesign was needed. The initial PT100 was read out in the 4-wire resistance mode of the *DMM6500*, which provided a measurement resolution and accuracy which was not needed for the required temperature control. As the *DMM6500* only has four separated input terminals, a

(a) Lens Temperature (b) Internal Housing Temperature (c) External Temperature (d) Bottom Housing Temperature

Figure 19: Temperature sensor positions on the PCAM.

multiplexing card needs to be used to enable the readout of multiple sensors, which connects the input terminals to different sensors in turn. In summary, implementing a 4-wire measurement for all 4 sensors would have significantly complicated the manufacture and readout, leading to an increased cost and unneeded complexity.

The Keithley multiplexing card *2000-Scan 172D* connects the different sensors to the input terminals with a bank of relays to influence the signal as little as possible. To protect these relays from unneeded wear, some care needed to be taken when writing the controller code to only read out the sensors which were actually needed.

5.2 Instrument Control

To be able to respond to changing external temperatures and to precisely control, a temperature controller is needed. Whilst this would have been implemented in a self-contained module in the final PCAM, for prototyping and testing, a *Raspberry Pi 5 Model B Rev. 1.0* was used to control the Digital Multimeter (DMM) and Power Supply (Unit) (PSU).

The raspberry is running the raspbian operating system and is accessed over ssh by default. The control code is written in python using the *pyvisa* package, which implements the Virtual Instrument Software Architecture (VISA) protocol specification.

Initially, the instruments were connected together over the local access network. As this connection was not stable and experiences frequent dropouts and timing errors, a robust control program was needed. At the start of the program, the instrument handler is initialized and connects to the instrument. To be robust against temporary connection dropouts, this connection attempt is repeated a set number of times (arbitrarily set to 3 here). If the connection is successfully completed, the main loop starts. In case three connection attempts are unsuccessful, the instrument is disabled and not queried in later program stages. As the temperature control does not function and the entire setup does not deliver any data without the DMM, the program only continues if only the PSU is disabled and stops if the connection to the DMM is broken.

The main loop first tests if the connection is still active by pinging the instrument. In case of a malformed or non-existent response, a new instrument handler (and thus a new connection) is initialized to try and recover normal operations. If the ping returns

as expected, the main loop has two sub-loops which run once a second and every twenty seconds respectively.

Running once a second, the heating control loop reads in the current lens temperature and calculates the needed heating power to reach the temperature setpoint (25 °C in normal operation). The regulation is implemented with a Proportinal Integral Derivative (PID) controller, which is described in more detail in subsubsection 5.2.1 The program then calculates the expected voltage and current output and set the PSU output accordingly. The current output is only set as a safety precaution, as the heater resistance does not change significantly from the nominal values in the temperature regimes this setup is expected to operate. To check if the set heating power is actually delivered, the PSU output power is queried and saved to a CSV file together with the measured lens temperature and the set output power. As the setup has a large thermal mass compared to the maximum heating power, it is sufficient to run the control loop once a second, as there are no relevant temperature changes on shorter timescales.

Running every twenty seconds, the data saving loop queries all four available temperature sensors and saves the results to a CSV file. To get a more reading stability, an integration time of 10 power line cycles is set. As the multiplexing card needs to switch between the channels mechanically, this full query is limited to run no faster than about once every 5 seconds. The readout time of 20 s was chosen as a comprimise to capture transient effects, not to unnecessarily increase the data file size and to reduce wear on the multiplexing card.

In addition to keeping the lens at a constant temperature, the program is able to run temperature sweeps with arbitrary temperature profiles, only limited by relying on heat conduction to the outside to cool down. In case a temperature sweep is required, a sweep plan needs to be set at the program start. The sweep is realized by changing the temperature setpoint before calculating the new required heating power. This feature was added to emulate the heating campaigns by Matzke, 2025, the results of which are discussed in section 3.

Either in case of a user keyboard interrupt, if the DMM is disabled or if some error is not caught (and is therefore not originating in the connection to the instruments), the program shuts the instruments down. This includes deactivating the PSU output to stop any heating effects and closing the connections to the active instruments. If this controlled shutdown is unsuccessful, the setup is most likely in an unrecoverable state, potentially even with power flowing into the heating resistors uncontrolled, and as such requires immediate human intervention. This can happen if an unrecoverable connection failure occurs when shutting down the program.

During operation, all errors and operation messages are saved in a log file to aid in later debugging.

A flowchart of the whole program is shown in Figure 20.

As persistent connection errors with the PSU requiring a powercycle continued to be an issue, which lead to multiple measurement campaigns to fail without any data. To avoid all network-related issues, the connection was switched to USB, which provided more stability with the drawback that now, the Raspberry Pi needs to be positioned close to the instruments. While this switch did make the connection more stable, the connection to the PSU still failed due to a timeout after 15 days of continuous operation, while the DMM continued with its datataking, running for 35 days at the time of writing. Whilst this shows that the setup is not stable long-term, it is robust enough for

validation campaigns of PCAM. Should a temperature stabilization system be required in the final PCAM, it would be implemented using hardwired logic and not prone to errors in the connection between controller and instruments.

5.2.1 PID Controller

The most common (and simplest) method of process control is with a PID controller, as it does not require any knowledge or modelling of the system to be controlled. A "textbook" PID controller can be written as (Astrom and Hagglund, 1995, Chap. 3)

$$u(t) = K\left(e(t) + \frac{1}{T_i}\int_0^t e(\tau)\mathrm{d}\tau + T_d\frac{\mathrm{d}e(t)}{\mathrm{d}t}\right) \tag{6}$$

with the control variable u the error term $e(t) = y_{\text{setpoint}} - y_{\text{measured}}$. K, T_i and T_d are tunable parameters which need to be set according to the system response to the control output. In our case, u represents a power output and $e(t)$ is the difference between the setpoint temperature of 25 °C and the measured temperature at the lens.

The simplest control case is that of purely proportional control, where $\lim \frac{1}{T_i} \to 0$ and $T_d = 0$. This causes the control output to be directly proportional to the control error. In most cases, strictly proportional control leads to steady-state offsets between the setpoint y_{setpoint} and the actual value y at $\lim t \to \infty$. (Astrom and Hagglund, 1995, Chap. 3.2)

To avoid this steady state error, the integral term is needed. Whenever there is a control error $e(t) \neq 0$, however small, the integral will counteract it and cause the error to decrease until zero. Where this causes problems is in systems with a long time delay between a control input and the system response. In that case, called *integral windup*, the integral term grows so large during the time where the system is approaching the setpoint, that the system overswings, causing windup in the other direction. This lead to long settling times or even oscillations. To counteract integral windup, limits are placed on the integral term (or the overall control output). (Astrom and Hagglund, 1995, Chap. 3.5)

The derivative term dampens the PID controller by linearly extrapolating the future error of the system and reducing the output accordingly. This reduces oscillations and overshoot in the system and is only needed in systems with a quick response to the control input. (Astrom and Hagglund, 1995, Chap. 3.3)

In real implementations of PID controllers, both integral and derivative are implemented numerically and thus have limited a limited time resolution. In addition, there are various different implementations which improve upon the "textbook" formula.

To control the setup for controlling the PCAM temperature, the python library *simple-pid* was used, which implements a PID controller with anti-windup in python. The PID parameters input into the controller do not map directly onto the simple formula given in Equation 6 due to the optimisations that were done during implementation.

The PID terms for the PCAM setup were tuned by placing it inside of a climate chamber at −10 °C and varying the default values systematically. To avoid an overheating of the solder joints and the camera internals and to limit integral windup, a maximum output power of 20 W was set. Though there exist rules of thumb for setting the parameters, the thermal mass makes these techniques time-consuming. The slow response made it possible to set the parameters one by one, first increasing the

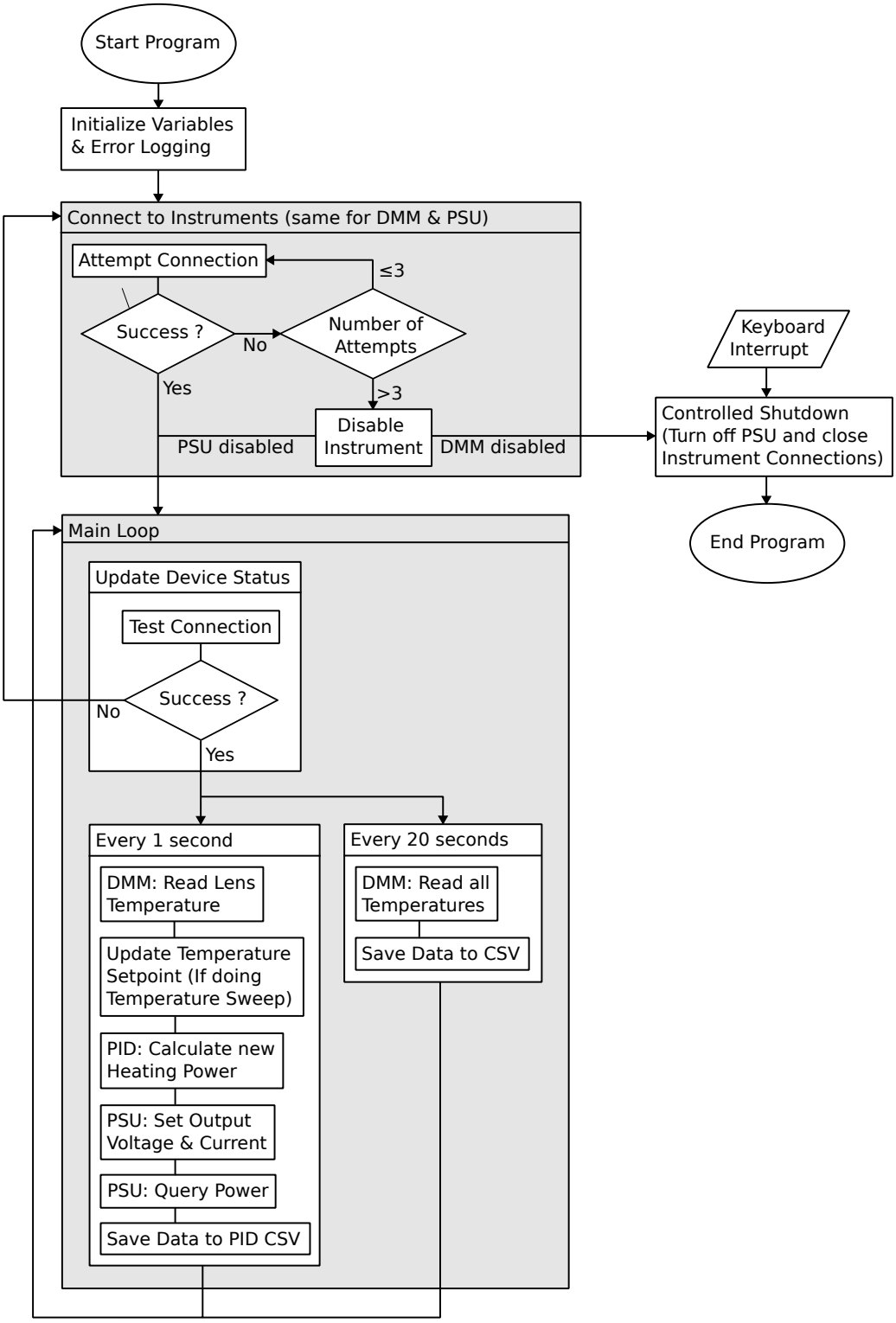

Figure 20: Instrument control flowchart.

proportional term until the system started heating at the limit of 20 W at a temperature differential of about 5 °C. This resulted in a steady-state error of about 1.5 °C, which was removed by increasing the integral term. As the overshoot was below 2 °C in the last test, which represents a worst-case scenario of a cold start at the absolute limit of the operating temperature envelope, the derivative term is not needed and set to 0.

The final PID parameters are $P = 5$, $I = 0.005$ and $D = 0$.

The step response of the controller was measured during a temperature sweep with both rising and falling steps of 2.5 °C. During the test, the external temperature was constant at (21.90 ± 0.05) °C. The temperature is said to be settled when it differs from the setpoint by no more than 0.1 °C for the last time. While the falling step took 254 s to reach this steady state, the falling step needed almost 4 times as long at 886 s. This may be due to residual heat energy slowly leaking into the temperature controlled area from the housing after the step. An exemplary step response for the step at $T_{\text{setpoint}} = 32.5$ °C is shown in Figure 21.

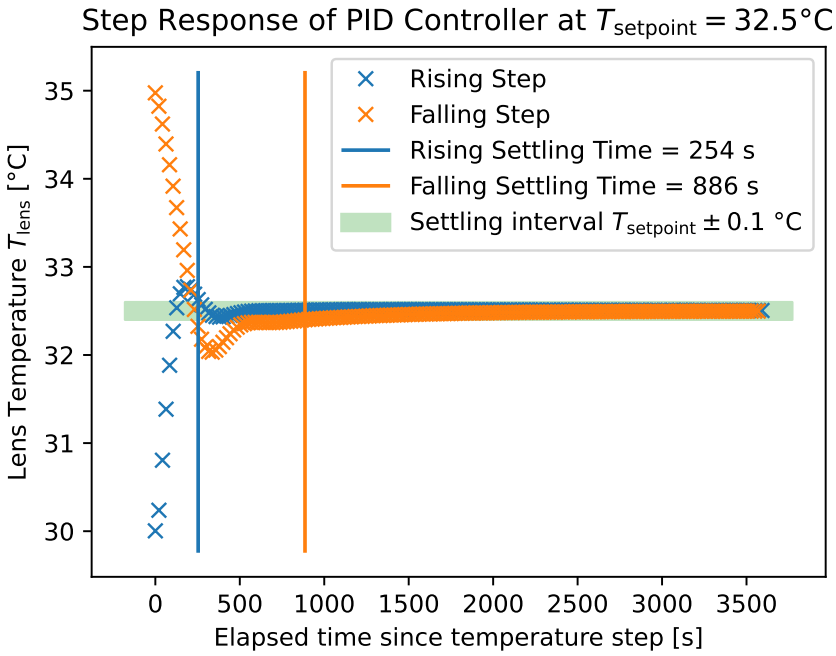

Figure 21: Falling and rising step response and settling times of PID controller at $T_{\text{setpoint}} = 32.5$ °C.

When looking at the stability against external temperature fluctuations, it is to be noted that the stabilization fails when the external temperature gets too close to the setpoint (here around 10 °C), as at that point the power input from the camera and the computer heats the internals over the temperature setpoint. This could only be avoided with active cooling or a higher setpoint. As active cooling would provide more complexity, a higher setpoint of 35 °C should be considered to avoid these problems at the higher end of the operating temperature envelope. When filtering the data to only consider a temperature differential $\Delta T > 10$ °C, the setup reaches a stability of $T_{\text{mean}} \pm \sigma_{\text{T}} = (25.00 \pm 0.01)$ °C.

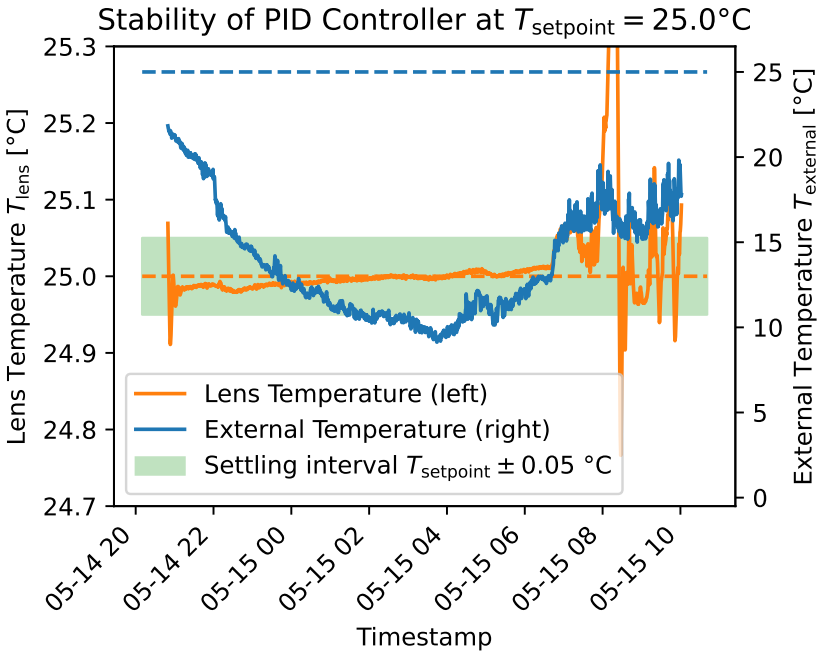

Figure 22: Temperature stability of PID controller at $T_{\text{setpoint}} = 25\,°\text{C}$ with fluctuating external temperature.

6 Lens Temperature Sweep

To both separate effects in the time and temperature domain and to check if the observed effects are actually caused by the lens, a temperature sweep was done by only heating the lens area using the setup described in section 5. In addition, a second external camera was mounted to the PCAM housing to check for effects caused by potential sagging of the tripod or astromount. The greater precision and stability of the temperature regulation archived with the PID controller both allowed smaller step sizes and a triangular stepwise sweep profile. With a step size of 2.5 °C and a range between room temperature around 23 °C and a maximum of 40 °C, an exploratory measurement yielded a settling time of at least 30 minutes. To ensure a complete steady state, each step was set to be 60 minutes in length, which allowed the filtering of the first 30 minutes after the setpoint change while still leaving enough data to have meaningful statistics. This resulted in the temperature and pointing traces shown in Figure 23. The missing parts were filtered out to only leave data in a steady state. A plot of the unfiltered data is shown in Figure 37 in the appendix.

The temperature sweep resulted in the pointing direction plot shown in Figure 30d. Due to a large amount of hysteresis, the pointing direction sweeps a circular shape during the temperature ramp.

A fit of the residual focal length and rotation was done, resulting in the fit parameters listed in Table 5 and the plot in Figure 24. The shown plot and fit use the lens temperature as their x axis. The respective plots and fit parameters for the camera, internal housing, external and bottom housing area temperatures are shown in subsubsection A.2.1 in the appendix. As expected, there is no dependence on the

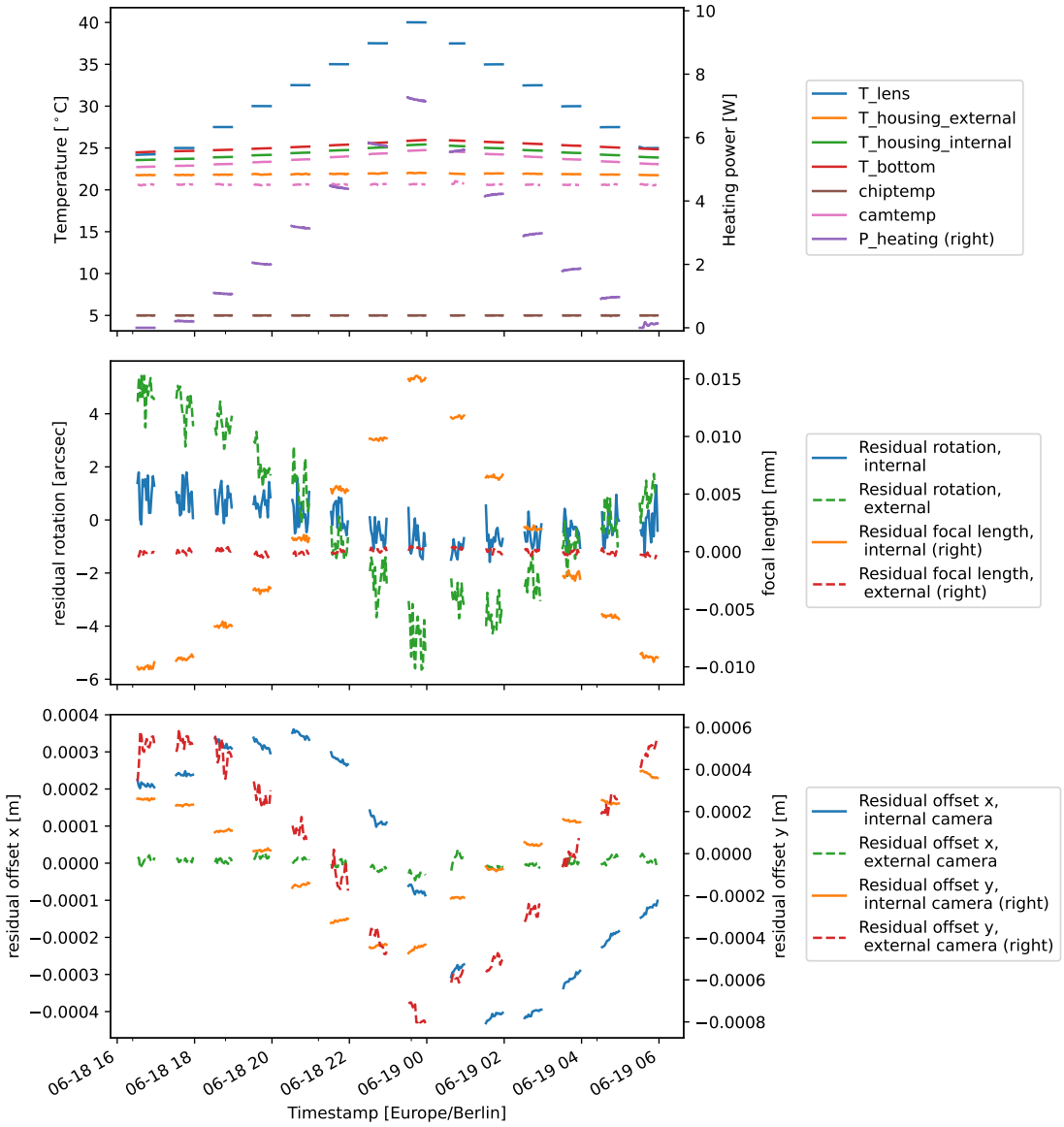

Figure 23: Overview of temperatures and pointing criteria for lens temperature sweep, filtered to only include measurements from steady-states.

external temperature, which was held almost constant ($\Delta T_{\text{external}} = 0.3\,°\text{C}$) by the lab air conditioning.

Fit value	Branch	Fit parameters ± fit uncertainty
Residual focal length	↑	$a = (158 \pm 6) \times 10^{-5}\,\text{mm}\,\text{K}^{-1}$
		$b = (-49.6 \pm 2.0)\,\text{mm}$
	↓	$a = (169 \pm 7) \times 10^{-5}\,\text{mm}\,\text{K}^{-1}$
		$b = (-52.1 \pm 2.1) \times 10^{-3}\,\text{mm}$
Residual rotation	↑	$a = (-0.112 \pm 0.014)\,\text{arcsec/K}$
		$b = (3.9 \pm 0.5)\,\text{arcsec}$
	↓	$a = (-0.083 \pm 0.009)\,\text{arcsec/K}$
		$b = (2.07 \pm 0.30)\,\text{arcsec}$

Table 5: Fit parameters of residual focal length and residual rotations with $T = T_{\text{lens}}$.

Comparing the fit parameters for the lens temperature to those of the previous heating campaign shows that they all differ by at least five standard deviations. Still, compared to the other temperature sensor positions, the lens temperature fit parameters are the only ones that fall within the same order of magnitude, with all other temperature sensor parameters being larger by at least one order of magnitude.

This might either be caused by general hysteresis or by the different temperature measurement point. The hysteresis would be caused by a remaining deformation in the PCAM after returning to a starting temperature. When doing the same fit with the camera temperature instead of the lens temperature and thus using the same temperature measurement point, the fit parameters are still significantly different. This is most likely mainly due to the much smaller temperature range that was archived at the camera temperature sensor ($\Delta T_{\text{lens}} = 15.8\,°\text{C}$ and $\Delta T_{\text{camera}} = 2.0\,°\text{C}$ compared to $\Delta T_{\text{camera}} = 24.3\,°\text{C}$ in the previous heating campaign).

A correlation analysis between the pointing data and the different temperature measurement points is done in section 8 to try to get an idea where the cause of the temperature dependence might be located.

As the data from the temperature sweep could be filtered to only include the respective steady states, a meaningful fit can be made for the focal length and residual rotation, shown in Figure 24. However, the data still shows significant hysteresis, which makes this fit only marginally useful to calibrate out the temperature dependence.

When plotting the pointing data onto an angular plane, the large amount of hysteresis produces an almost circular trace, shown in Figure 26.

7 Pointed campaigns with platesolving

To test the temperature stabilization in an real-world usecase, tests were done pointing the PCAM in a fixed direction and taking images. The resulting images were put through the solving pipeline described in subsubsection 2.4.1.

Four campaigns relevant to this work were performed:

- Roof campaign 1: on ECAP roof, stabilized to $T_{\text{lens}} \pm \sigma_{\text{T}} = (24.993 \pm 0.006)\,°\text{C}$, maximum distance from mean $^{+0.010\,°\text{C}}_{-0.014\,°\text{C}}$, PCAM housing placed directly on roof

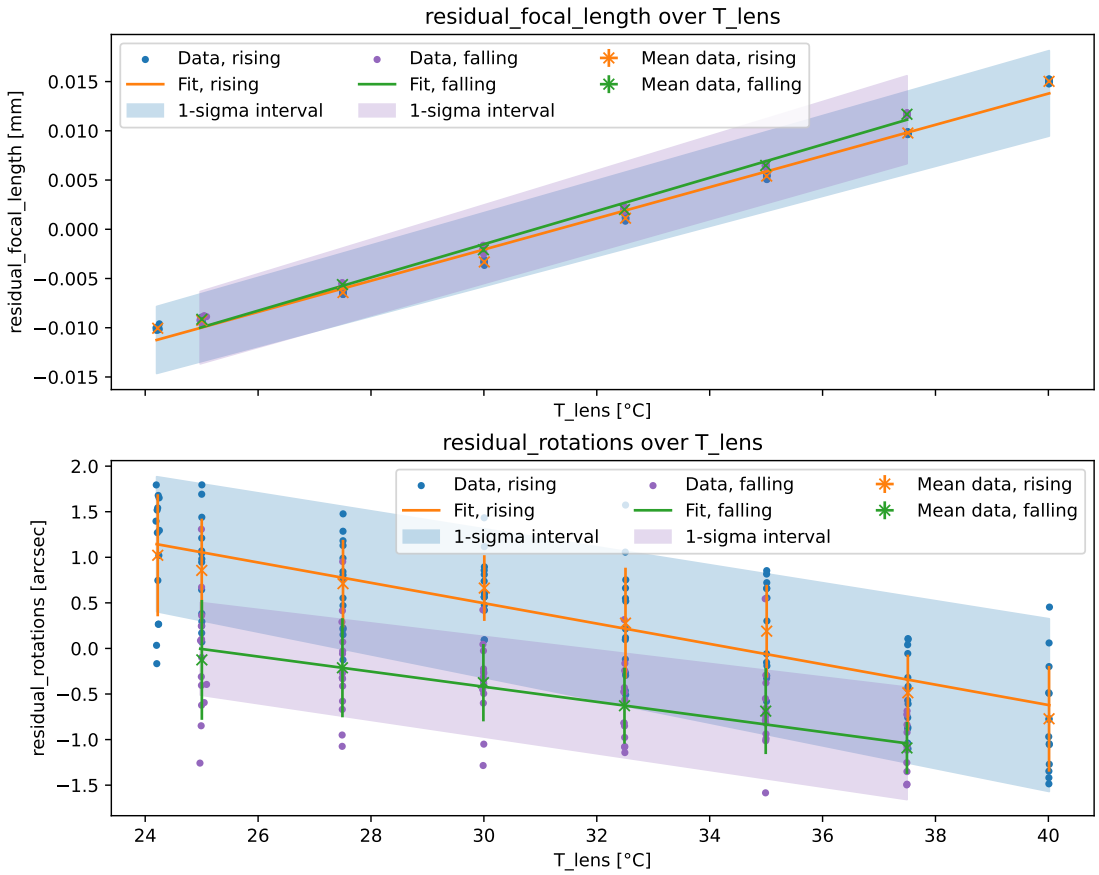

Figure 24: Fit of residual focal length and residual rotation using steadystate-filtered data from lens temperature sweep.

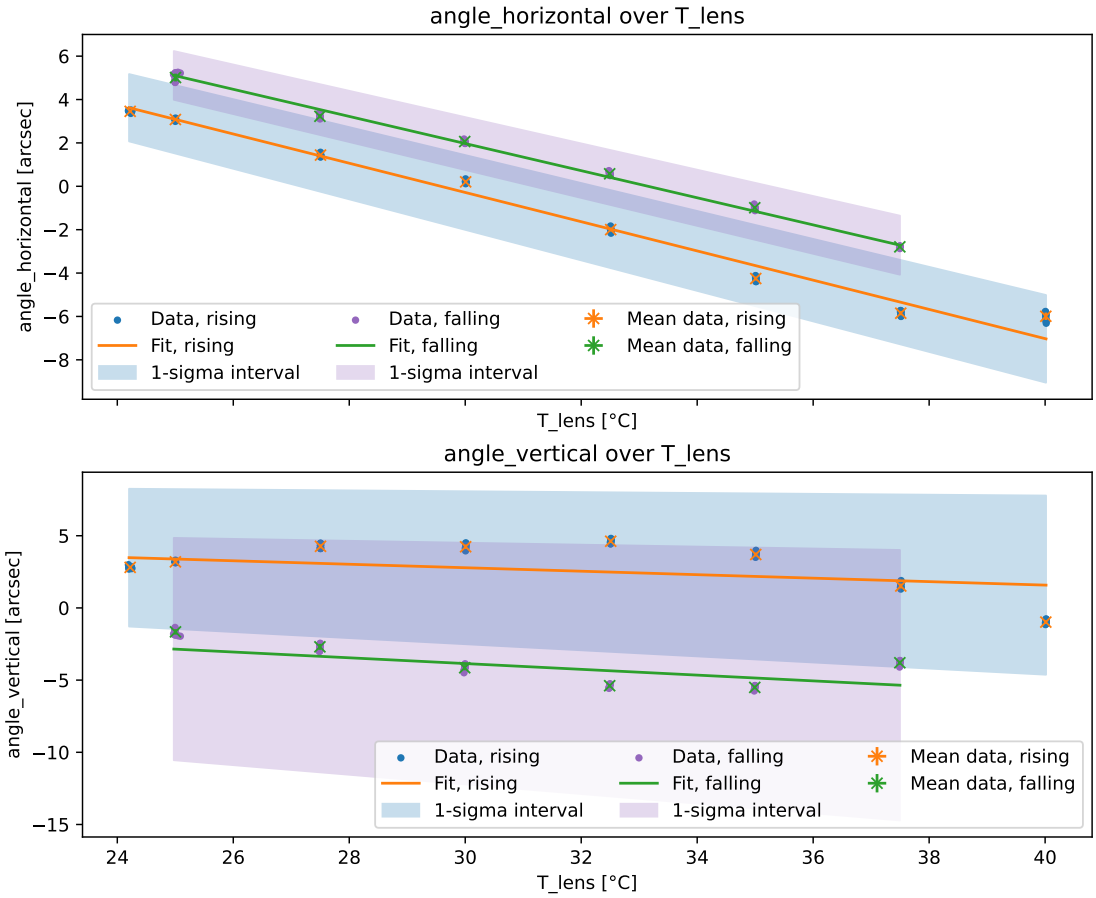

Figure 25: Fit of residual vertical and horizontal pointing angle using steadystate-filtered data from lens temperature sweep.

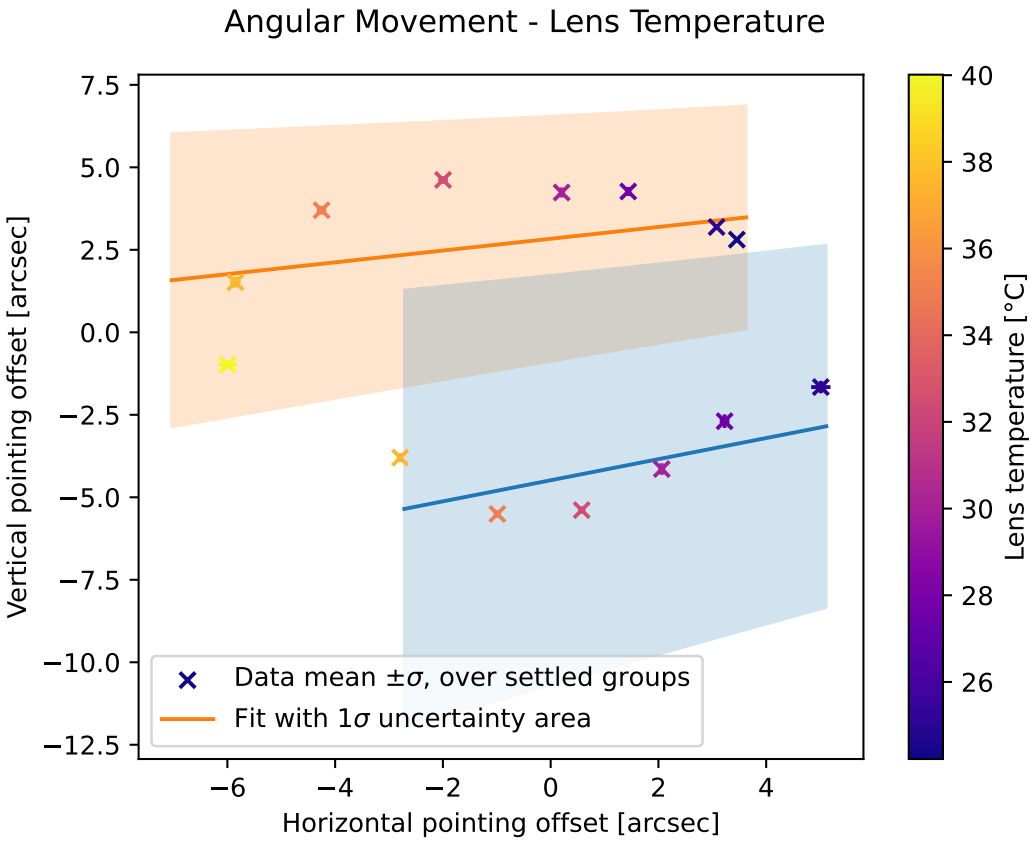

Figure 26: Fit of residual vertical and horizontal pointing angle on the angular plane using means of steadystate-filtered data grouped by temperature setpoint from lens temperature sweep.

tiles with wooden block

- Roof campaign 2: on ECAP roof, stabilized to $T_{\text{lens}} \pm \sigma_{\text{T}} = (24.994 \pm 0.005)\,^{\circ}\text{C}$, maximum distance from mean $^{+0.012\,^{\circ}\text{C}}_{-0.009\,^{\circ}\text{C}}$, PCAM mounted onto astromount and tripod on roof tiles

- Office campaign: in office through open window, stabilized to $T_{\text{lens}} \pm \sigma_{\text{T}} = (24.995 \pm 0.006)\,^{\circ}\text{C}$, maximum distance from mean $^{+0.015\,^{\circ}\text{C}}_{-0.015\,^{\circ}\text{C}}$, PCAM mounted onto astromount and tripod placed onto stable concrete floor

The setups for the *roof 1* and *office* campaigns are shown in Figure 28. The *roof 2* campaign was identical as in the office (except for the lack of an external camera on the roof) with the tripod legs placed onto three separate roof tiles (tiles visible in the background of Figure 27a).

(a) Roof 1

(b) Office, taken by Schaefer, 2025

Figure 28: Setups for the *roof 1* and *office* campaigns.

In the *roof 2* campaign, two outliers resulting from the tailing end of a series of clouded images were removed from the dataset. The resulting overview is shown in Figure 29.

The overviews of all datasets are shown in subsection A.2 in the appendix. In all the campaigns, the external temperature decreased over the duration of the measurement series. *Roof 1* and *2* include breaks when no pointing data is available, which is caused by a temporary increase in the cloud cover obscuring the stars needed for plate solving. During these breaks, an increase or plateau in the external temperature is visible, which

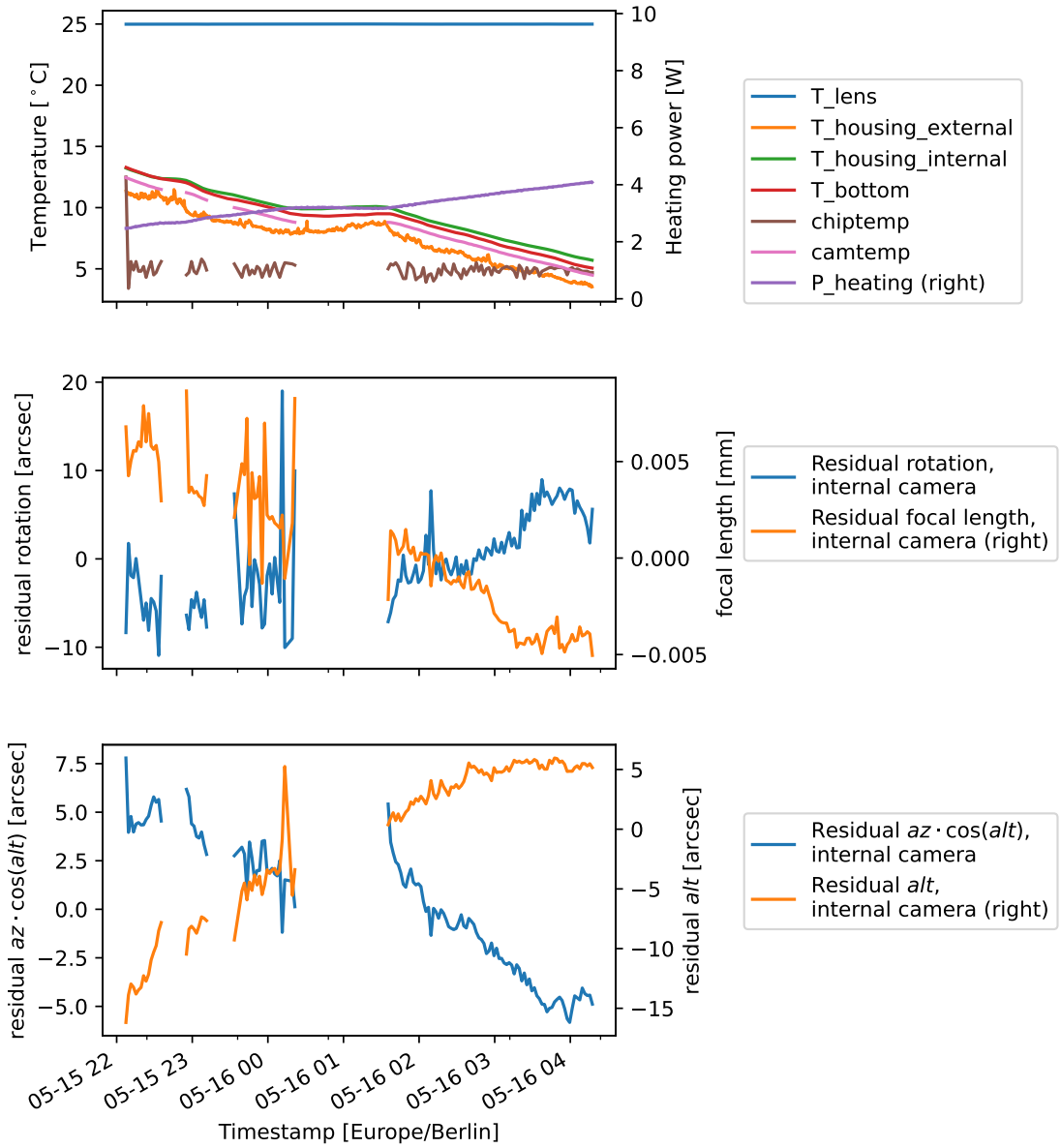

Figure 29: Overview of temperatures and pointing criteria for *Roof 2* campaign filtered to remove two outliers and including breaks without pointing data caused by clouds.

is explained by an increase of the IR radiation emitted by the atmosphere (in this case, the clouds radiate more than the clear sky) (*Clouds Do Not "Act Like Blankets"* 2024).

When comparing the movement of the different campaigns shown in Figure 31, some distinct characteristics can be seen:

The change onto the tripod reduced the temperature-induced drift by more than a factor of two. As the difference between the maximum and minimum temperature stayed roughly the same (8.0 °C and 8.9 °C respectively), this is most likely not due to the different temperature ranges but to to an external influence. This points out a problem with both campaigns on the ECAP roof, in that changes of the external temperature cause the ground structure to deform and in turn move the PCAM. The diagonal trend from top left to bottom right (though reversed in direction) in Figure 30a and Figure 30b is thus assumed to be mainly due to external influences.

To further limit the influence of the ground on the pointing direction, the setup was moved to an office with a solid concrete floor. The images were taken out of an open window to both eliminate possible refractions and reflections in the glass and enable the external temperature to reach the PCAM. This campaign shows a much smaller correlation between the vertical and horizontal angles (Spearman's rank correlation coefficients of $r_{\text{office}} = -0.57$ compared to $r_{\text{roof1}} = -0.98$ and $r_{\text{roof2}} = -0.87$) and a smaller overall spread.

The mean and maximum residual distances from the mean pointing position are shown in Table 6. As the use of the standard deviation to gauge the spread of the pointing direction is problematic in this case, as the pointing directions have some underlying non-gaussian distribution due to the temperature dependence, the maximum residual distance is also given.

Parameter	Campaign	Value ± std
Mean residual distance from pointing mean $d \pm \sigma_{\text{d}}$	Roof 1	(15 ± 10) arcsec
	Roof 2	(6 ± 4) arcsec
	Office (internal)	(5 ± 3) arcsec
	Office (external)	(50 ± 40) arcsec
	Temperature sweep (internal)	(5.1 ± 0.6) arcsec
	Temperature sweep (external)	(4.8 ± 2.8) arcsec
Maximum residual distance from pointing mean Δd_{max}	Roof 1	35 arcsec
	Roof 2	18 arcsec
	Office (internal)	14 arcsec
	Office (external)	17×10^1 arcsec
	Temperature sweep (internal)	6.1 arcsec
	Temperature sweep (external)	9.7 arcsec

Table 6: Pointing spread parameters for pointed campaigns and temperature sweep.

The focal length deviates by a similar amount in all pointed campaigns and the temperature sweep. In the external camera of the temperature sweep, the spread is smaller by and order of magnitude, which is expected as this camera was entirely coupled

to the stable room temperature. The jump in the focal length mean after the both roof campaigns is due to a refocussing of the PCAM after reassembly.

Parameter	Campaign	Value ± std
Mean focal length $f \pm \sigma_\mathrm{f}$	Roof 1	(51.857 ± 0.004) mm
	Roof 2	(51.855 ± 0.004) mm
	Office (internal)	(51.6893 ± 0.0028) mm
	Office (external)	(51.657 ± 0.004) mm
	Temperature sweep (internal)	(51.725 ± 0.008) mm
	Temperature sweep (external)	$(51.660\,00 \pm 0.000\,25)$ mm
Maximum deviation from mean Δf_max	Roof 1	$+0.010$ mm, -0.006 mm
	Roof 2	$+0.009$ mm, -0.005 mm
	Office (internal)	$+0.0071$ mm, -0.0066 mm
	Office (external)	$+0.009$ mm, -0.007 mm
	Temperature sweep (internal)	$+0.013$ mm, -0.013 mm
	Temperature sweep (external)	$+0.000\,51$ mm, $-0.000\,59$ mm

Table 7: Focal length spread for pointed campaigns and temperature sweep.

The rotation of the temperature dependence between Figure 30a, Figure 30a and Figure 30c is due to a 180° rotation of the PCAM setup in the *roof 2* campaign compared to the two others.

The same linear fits of the temperature dependence of the pointing parameters as in section 6 were done with the data from the three campaigns. For the fits, the raw data was binned in increments of 1 °C in the camera temperature and the mean and standard deviation calculated.

The fit paramters are listed in Table 8. For the temperature sweep, the residual *alt* represents the vertical and the residual $az \cdot \cos(alt)$ horizontal angle. The sign of the *roof 2* campaign is flipped due to the different camera orientation in relation to the celestial axes compared to the other two campaigns.

In the temperature sweep, the effect of the camera temperature on the focal length is larger by an order of magnitude, potentially due to the temperature differential created by only heating the lens. When comparing with the fit parameters from the heating campaign of Matzke, 2025 previous to this work, where too the entire camera was heated from the outside, they are in the same order of magnitude, though still slightly smaller here. This may be explained by the overall higher temperature range from the previous work. Why the focal length temperature dependence has a different sign in the *office* campaign is unclear.

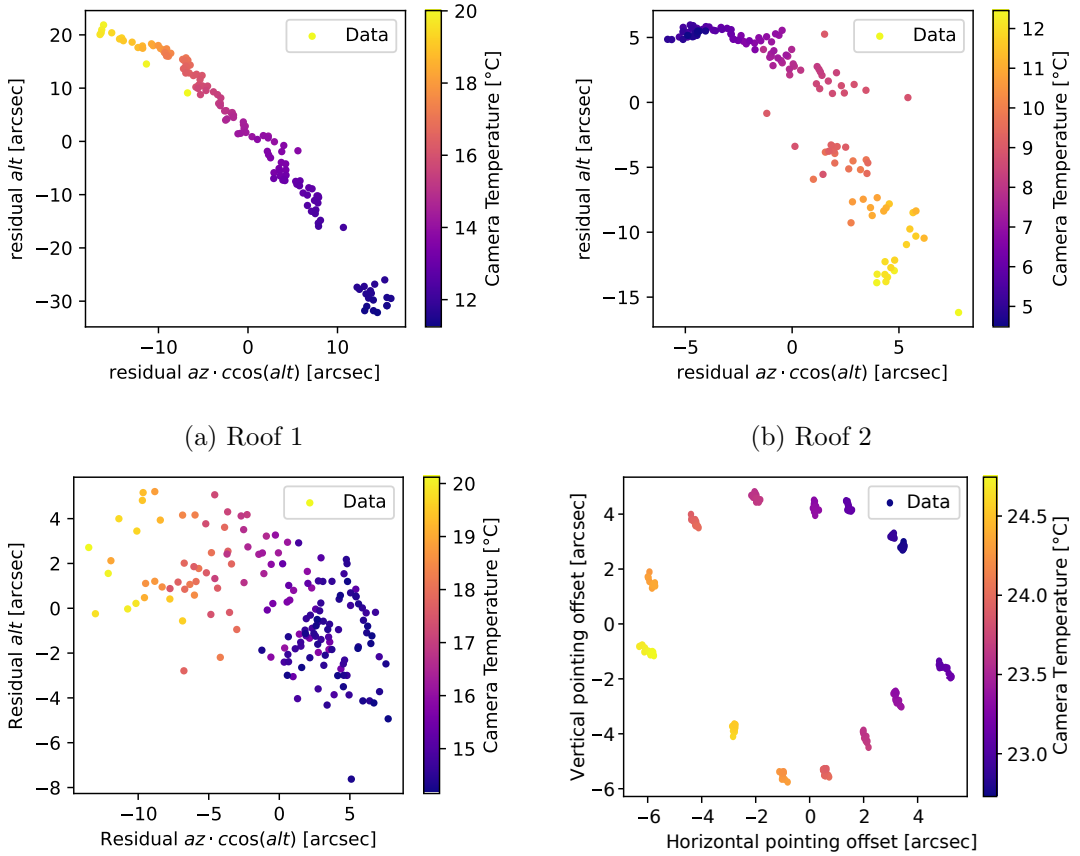

(a) Roof 1

(b) Roof 2

(c) Office

(d) Temperature Sweep (Lab)

Figure 31: Pointing direction residuals from different measurement runs.

	Focal length $[10^{-5}\mathrm{mm\,K^{-1}}]$ $a_\mathrm{f} \pm \sigma_\mathrm{a}$	Rotation $[10^{-5}\mathrm{deg/K}]$ $a_\mathrm{rotation} \pm \sigma_\mathrm{a}$	Residual alt [arcsec/K] alt $a_\mathrm{alt} \pm \sigma_\mathrm{a}$	Residual $az \cdot \cos(alt)$ [arcsec/K] $a_{\mathrm{az\ cos(alt)}} \pm \sigma_\mathrm{a}$
Temperature Sweep	1312 ± 21	-25.8 ± 2.2	-1.4 ± 0.8	-5.8 ± 0.4
Roof 1	131 ± 11	154 ± 19	5 ± 1	-3.29 ± 0.23
Roof 2	151 ± 12	-49 ± 7	-2.6 ± 0.4	1.47 ± 0.07
Office (internal)	-44 ± 6	-43 ± 13	0.6 ± 0.4	-2.87 ± 0.11

Table 8: Fit parameters of pointing parameters for pointed campaigns and temperature sweep ($T = T_\mathrm{camera}$).

8 Correlation Analysis

8.1 Spearman's rank correlation coefficient and Pearson correlation coefficient

To get hints to where the temperature dependence might be located, a correlation coefficient is calculated for the different pointing criteria and measured temperatures. Here, Spearman's rank correlation coefficient (SRCC) is used to gauge how well the relation could be described by a monotonic function. At first, Pearson correlation coefficient (PCC) was used, but was replaced as to not limit the analysis to linear relations, though most correlation coefficients stayed the same to $\pm 10\,\%$.

The Spearman's rank correlation coefficient was used, as the temperature dependencies are expected to be monotonic for the small temperature ranges which were able to be tested when simultaneously getting pointing directions from the LED lab setup or plate solving.

The Spearman's rank correlation coefficient indirectly used the Pearson correlation coefficient, but applies its formula to the rank of the data.

The rank $rg(x_i)$ of a value x_i is its position j in a sorted list of all x values such that the $x_{(1)} \leq x_{(2)} \leq \ldots \leq x_{(n)}$, with $x_{(j)}$ being the value of x with rank j. In case of duplicate values, the arithmetic mean of the rank of the group of duplicates gets assigned to all of them. Thus, each datapoint (x_i, y_i) gets converted to a rank $(rg(x_i), rg(y_i)$ and the Pearson correlation coefficient applied to this dataset. (Fahrmeir et al., 2023, Chap. 3.4.2)

The Pearson correlation coefficient of parameters X and Y is defined as

$$r_{\mathrm{XY}} = \frac{\sum_{i=1}^{n}(x_i - \bar{x})(y_i - \bar{y})}{\sigma_{\mathrm{X}}\sigma_{\mathrm{Y}}} \tag{7}$$

with the standard deviations

$$\sigma_{\mathrm{X}} = \sqrt{\frac{1}{n}\sum_{i=1}^{n}(x_i - \bar{x})} \quad \text{and} \quad \sigma_{\mathrm{Y}} = \sqrt{\frac{1}{n}\sum_{i=1}^{n}(y_i - \bar{y})} \tag{8}$$

This produces values in the range $[-1; +1]$ and gives a measure of how strongly X and Y are linearly correlated with each other. The values are roughly grouped into the categories of *weak* ($|r| < 0.5$), *moderate* ($0.5 \leq |r| < 0.8$) and *strong* ($0.8 \leq |r|$) correlation. (Fahrmeir et al., 2023, Chap. 3.4.1)

While the restriction to only consider monotonic relations is certainly limiting and the data, especially considering hysteresis, does show non-monotonic relationships, this approach was taken to try and inform a sensor placement with which a temperature compensation can be realized. In general, the correlation coefficients are only to be taken as an indication, where an causal effect may be found and not as direct evidence for this effect in itself. To prove that a correlation follows from a causation in this setup further measurements and modelling is needed. Furthermore, the correlation coefficients give no indication of the relative strengths of the effects, in that one temperature might have a very small effect on a parameter but be perfectly correlated, while being overshadowed by a larger effect which is only weakly or moderately correlated.

8.2 Correlation coefficients of pointing criteria

8.2.1 Temperature Sweep

When looking at the Spearman's rank correlation coefficients for the temperature sweep in the lab and comparing the internal and external camera, it is clear that the external camera is influenced by the (internal) camera temperature only slightly. The rotation was moderately correlated to the bottom temperature and the timestamp in both cameras, which coincides with a strong correlation of the bottom temperature and the timestamp ($r = 0.98$). As such, this might have been caused by the mounting settling a bit during the measurement run, as the external camera was mounted onto the housing of the PCAM.

The weaker correlation for the external camera was expected, as the swept temperature was controlled for the internal lens and influenced the external camera only very little.

For the internal camera, the focal length is very strongly correlated to the camera temperature ($r = 0.98$), while the camera temperature itself is only weakly correlated to all other measured temperature. As such, placing an additional temperature sensor in the direct vicinity of the camera temperature sensor would give more precise data in following measurement campaigns. Placing a sensor closer to the potential root of the temperature dependence might eliminate the hysteresis, which may be caused by the time delay of a heat input propagating through the PCAM housing. The corresponding correlation plots are shown in subsubsection A.3.1 in the appendix.

8.2.2 Pointed campaigns

In the pointed campaigns (*roof 1*, *roof 2* and *office*) all the temperatures except the lens temperature (which was held steady at $T_{\text{lens, mean}} \pm \sigma_{\text{T}} = (25.0 \pm 0.1)\,^{\circ}\text{C}$ for *roof 1* and *roof 2*) are strongly correlated to each other ($r \geq 0.79$), which is expected as the entire PCAM housing just followed the external temperature fluctuations. The temperatures are also strongly negatively correlated to the timestamp, as the temperature was falling during the nights of the campaigns. While the actual measured external temperature is only moderately correlated to the timestamp, this is explained by the random fluctuations of the external temperature on a short timescale which are caused by random air movement and smoothed over by the thermal mass of the PCAM.

The Spearman's rank correlation coefficients for the *roof 2* and *office* campaigns are shown in Figure 35. When comparing these two campaigns, the main difference in the correlation strength is that the altitude residuals are less strongly correlated to the external (and external-coupled) temperatures, as this correlation was partly caused by the unstable ground. The corresponding correlation plots are shown in subsubsection A.3.2 in the appendix.

In summary, it can be cautiously concluded from the correlation analysis:

- Most of the temperature dependence comes from an internal part of the PCAM (as the external camera shows less correlation than the internal camera).

- The cause for the focal length change may lie somewhere in the vicinity of the camera temperature sensor (as this temperature is very strongly correlated with the focal length).

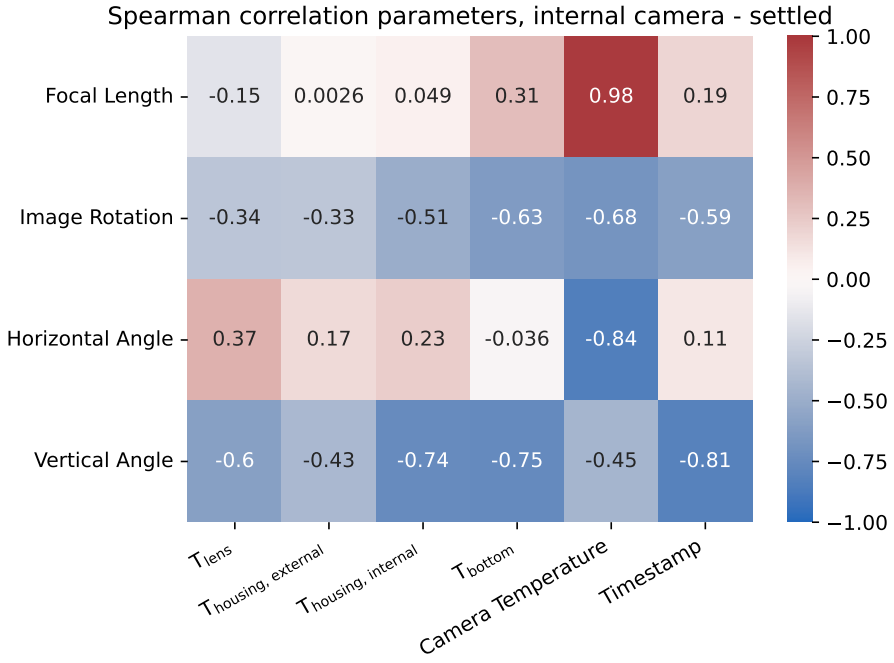

(a) Internal

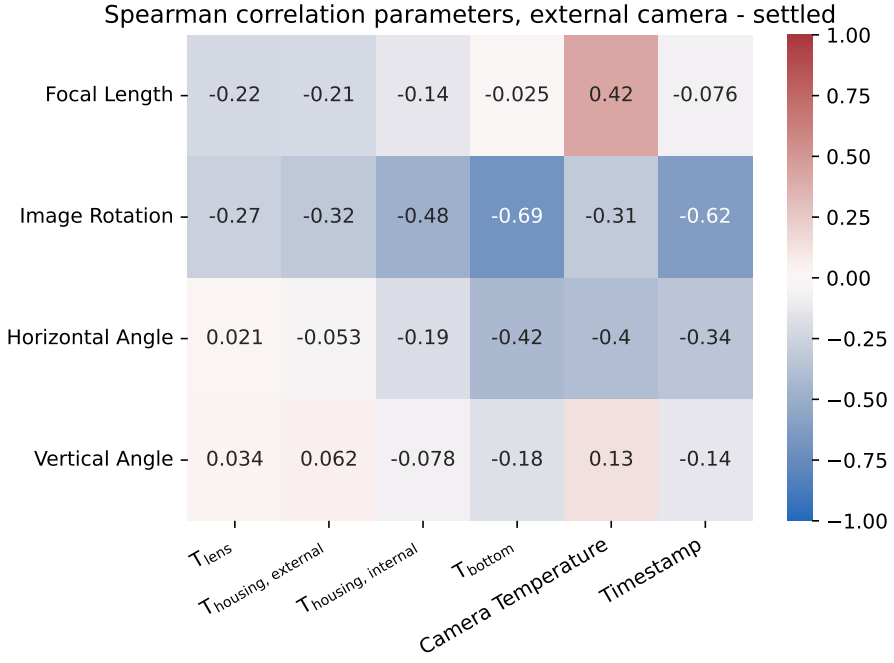

(b) External

Figure 33: Spearman's rank correlation coefficient of pointing parameters and temperatures in settled states during laboratory temperature sweep.

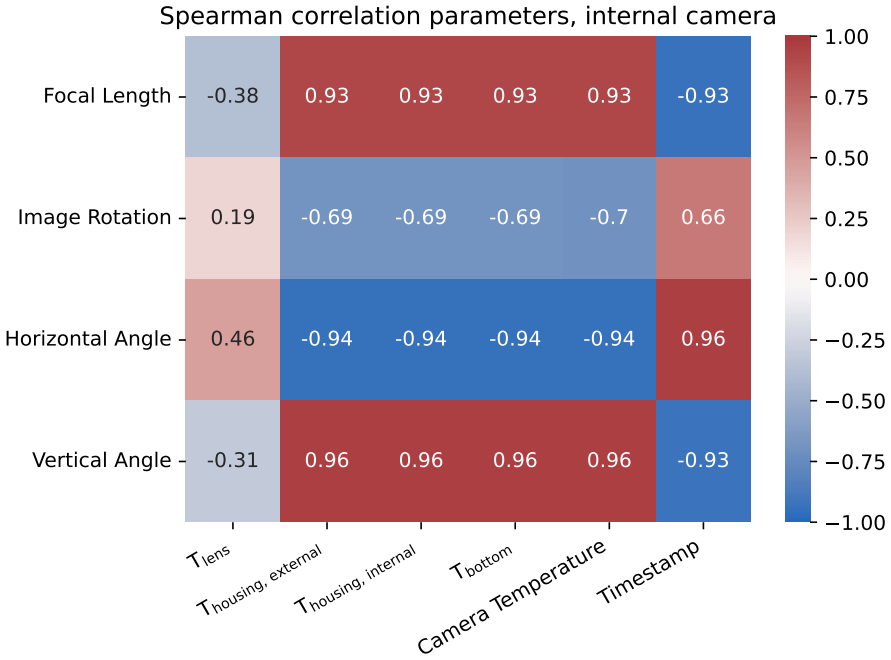

(a) Roof 2

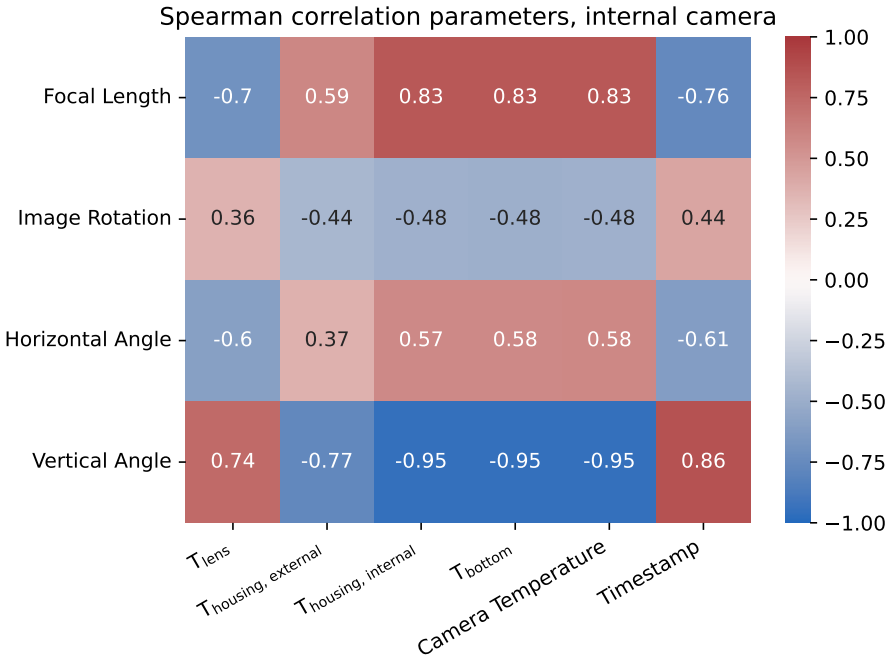

(b) Office

Figure 35: Spearman's rank correlation coefficient of pointing parameters and temperatures in pointed campaigns.

- There is no clear indication where the source of the temperature dependence of the pointing direction (as no single temperature sensor was significantly more correlated to the pointing direction).

9 Summary and Outlook

A scalable system to read out multiple temperature sensors and stabilize the temperature of the PCAM lens to $(25.00 \pm 0.01)\,^{\circ}\mathrm{C}$ while staying within the power budget of the PCAM was developed. When used during camera operation when the internal components are producing additional heat, this goal is reached for a setpoint at least $10\,^{\circ}\mathrm{C}$ above the ambient temperature. This system is stable for measurement runs on timescales of a few days, but occasionally fails due to connection errors to the instruments. As such, a more permanent setup would be needed for deployment in production, optimally implementing the temperature controller as a standalone circuit block.

By running a temperature sweep of the setpoint of the lens temperature in a laboratory environment, a temperature dependence of the focal length, image rotation and pointing direction of the PCAM was quantified.

Together with the data from three pointed campaigns, individual linear fits were done in an attempt to produce calibration values for this temperature dependence. This was unsuccessful, as the temperature ranges in the pointed campaigns significantly smaller than the required operating temperature range of the PCAM and the temperature sweep of the lens temperature did not yield representative results for actual operation.

Correlation analysis of the measured temperatures and the pointing parameters cautiously shows that the temperature dependence is likely caused by components internal to PCAM, though a stable mount and ground are still needed to produce workable results. Furthermore, while the cause of the focal length change may lie in the vicinity of the camera temperature sensor, no such position was able to be discerned for the pointing direction and image rotation.

This work shows that a temperature stabilization of the lens in itself is not sufficient to suppress the temperatures dependence and scattering of the pointing parameters. To archive the pointing criteria required for the Medium-Sized Telescope, either the whole PCAM needs to be temperature-stabilized or the actual source of the temperature dependencies needs to be found. Should the source of the temperature dependence be found and no calibration be feasible, the developed setup can be used to immediately implement a temperature stabilization and validate this finding.

For further measurements, both more temperature sensor positions (both in the PCAM housing and inside the astrocam housing) need to be realized and ideally, a way to do temperature sweeps over the whole operating temperature range need to be done in a controlled manner while pointing parameters are measured. The addition of more temperature sensors is underway at the time of writing. For the wholistic temperatures sweeps, a temperature chamber would need to be modified in such a way that the PCAM was able to look out towards the LED ring pointing target. Moreover, an easy to access location for running further pointed campaigns with a stable ground for the tripod or a different stable mounting option is needed for validation of future changes or calibration attempts.

Acronyms

AGN Active Galactic Nuclei.

ASA Air Shower Array.

CORSIKA Cosmic Ray Simulations for Kascade.

CR Cosmic ray.

CTAO Cherenkov Telescope Array Observatory.

DMM Digital Multimeter.

EAS Extensive Air Showers.

EBL Extragalactic Background Light.

ECAP Erlangen Center for Astroparticle Physics.

Fermi-LAT Fermi Large Area Telescope.

FlashCam FlashCam.

FoV Field of View.

GCS Galactic Centre Survey.

GPS Galactic Plane Survey.

GR gamma ray.

H.E.S.S. High Energy Stereoscopic System.

IACT Imaging Air Cherenkov Telescope.

ISM Interstellar Medium.

KSP Key Science Project.

LHAASO Large High Altitude Air Shower Observatory.

LST Large-Sized Telescope.

MAGIC Major Atmospheric Gamma Imaging Cherenkov Telescopes.

MST Medium-Sized Telescope.

MSTCam MST-Camera.

PCAM Pointing Camera.

PCC Pearson correlation coefficient.

PID Proportinal Integral Derivative.

PMT Photo Multiplier Tube.

PSF Point Spread Function.

PSU Power Supply (Unit).

PWN Pulsar Wind Nebula.

SMBH Super-Massive Black Hole.

SNR Supernova Remnant.

SRCC Spearman's rank correlation coefficient.

SST Small-Sized Telescope.

SWGO Southern Wide-field Gamma-ray Observatory.

UHEGR Ultra High Energy Gamma Ray.

VERITAS Very Energetic Radiation Imaging Telescope Array System.

VHE Very High Energy.

VISA Virtual Instrument Software Architecture.

A Appendix

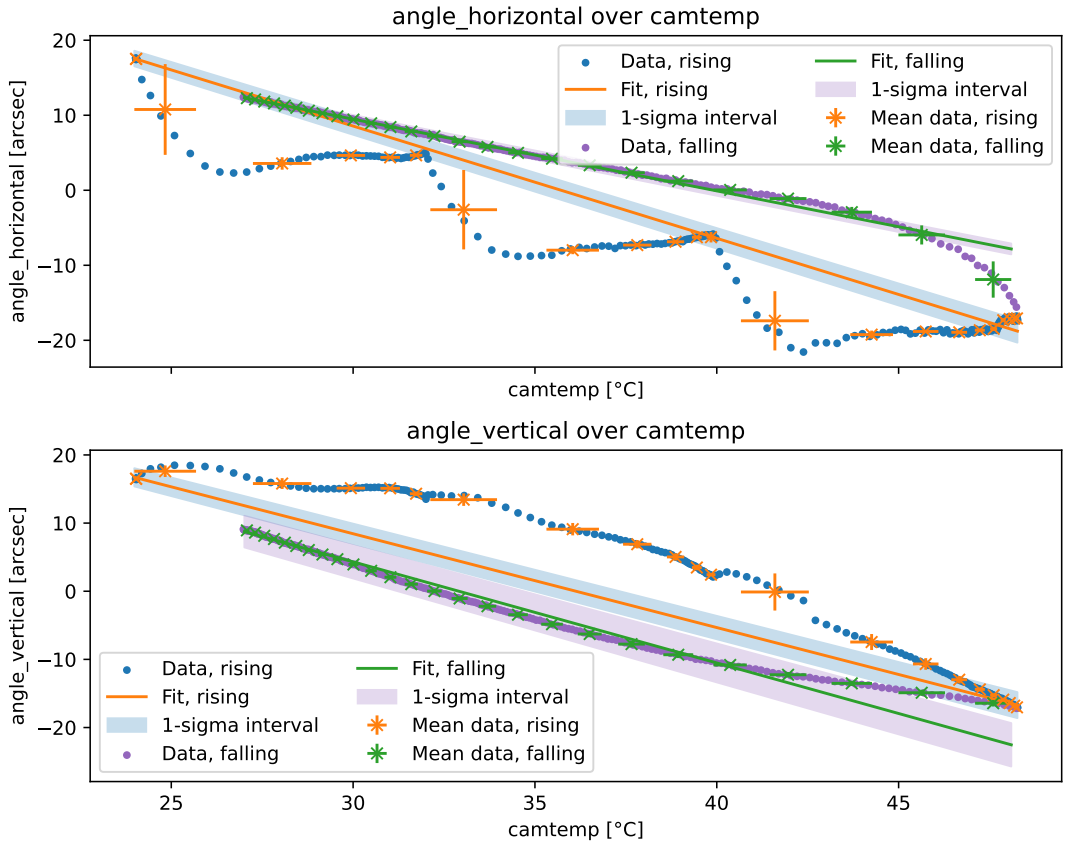

Figure 36: Horizontal and vertical pointing angle of PCAM when heating the camera housing from the outside in three steps (Data from Matzke, 2025).

A.1 Temperature Sweep

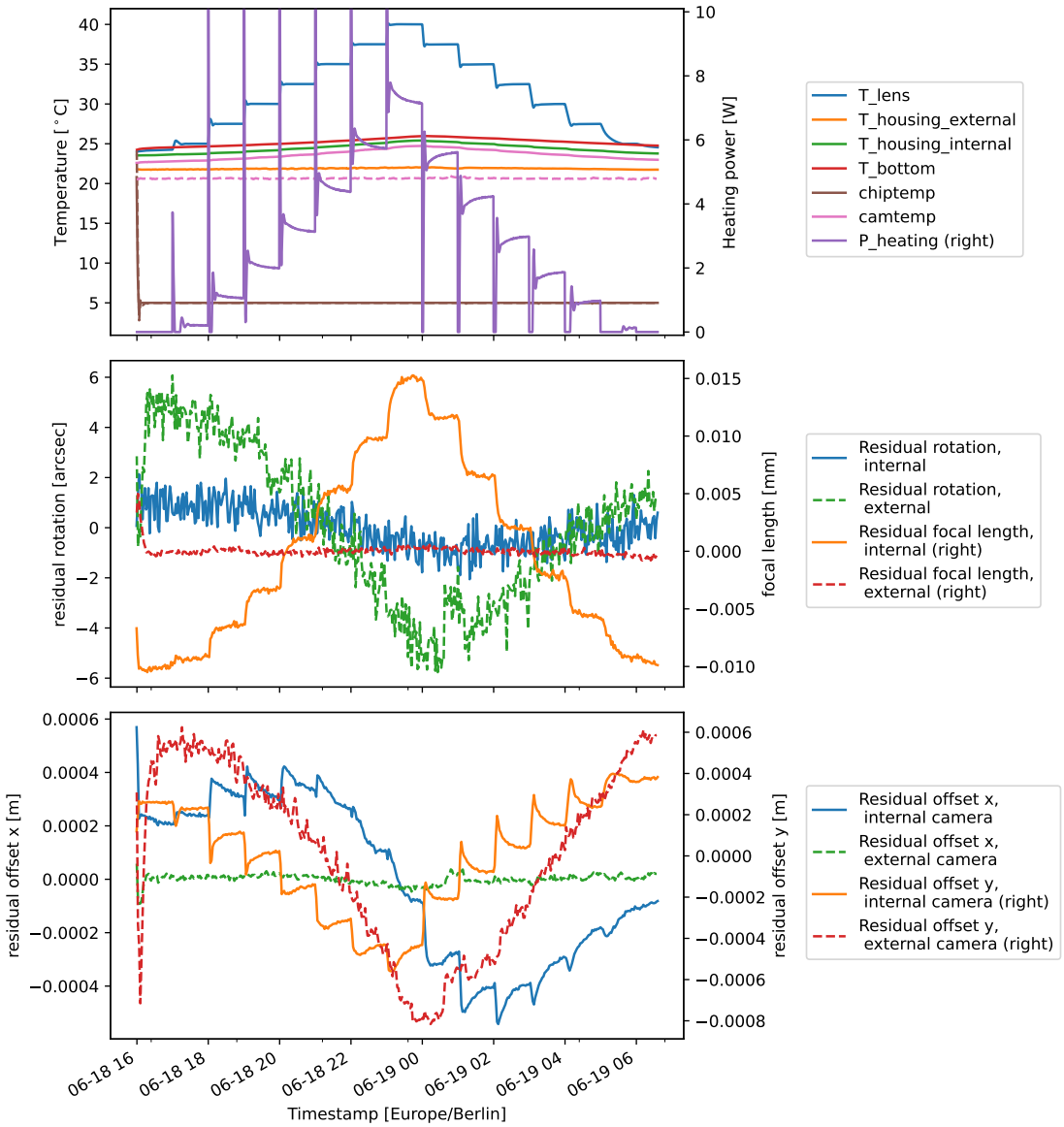

Figure 37: Complete overview of temperatures and pointing criteria for lens temperature sweep without filtering to settled states.

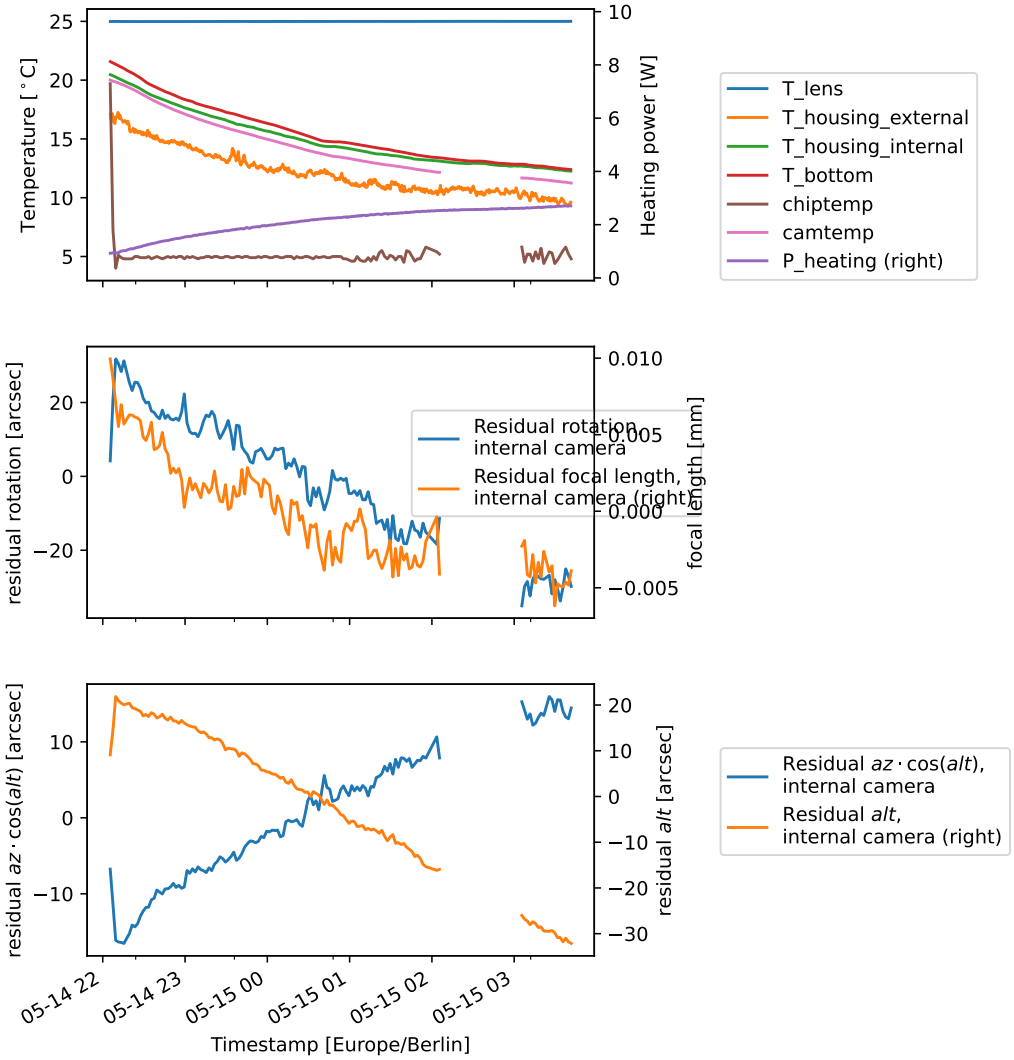

Figure 38: Overview of temperatures and pointing criteria for *Roof 1* campaign, including breaks without pointing data caused by clouds.

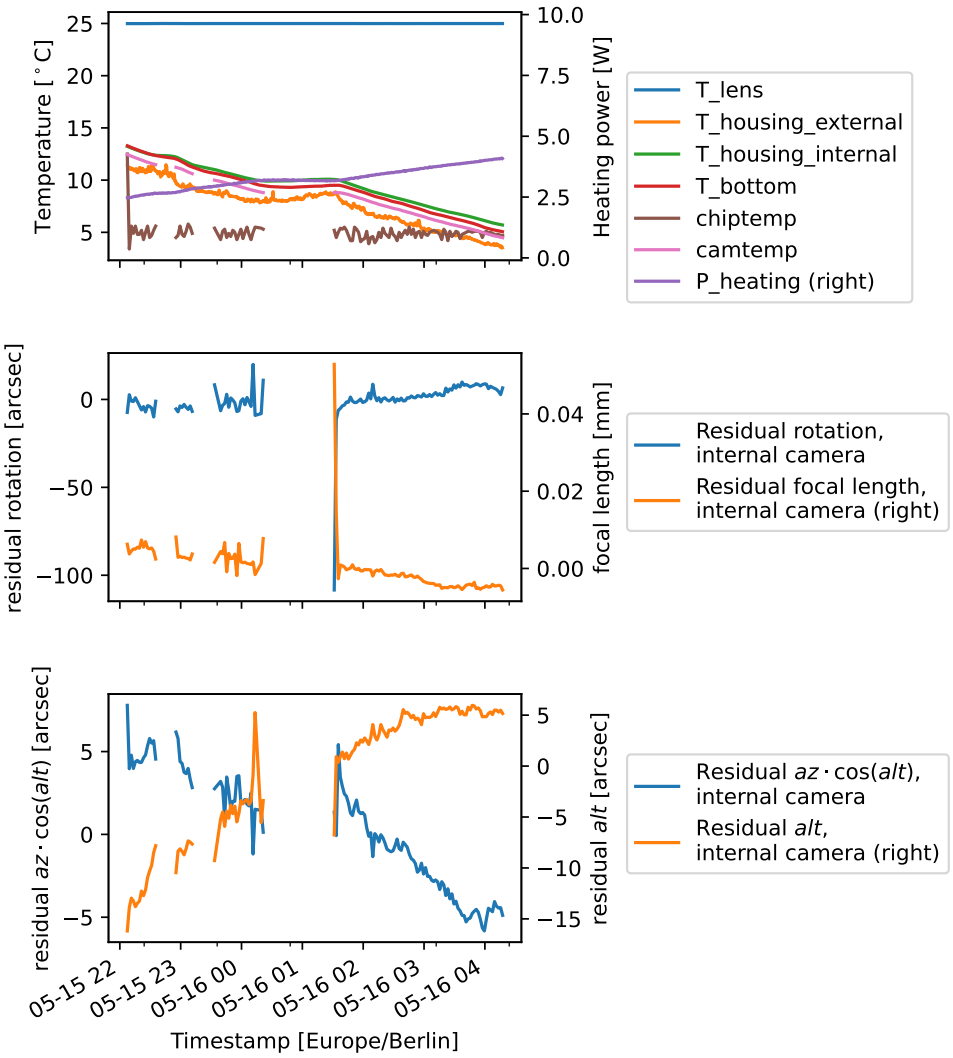

Figure 39: Overview of temperatures and pointing criteria for *Roof 2* campaign, including outliers and breaks without pointing data caused by clouds.

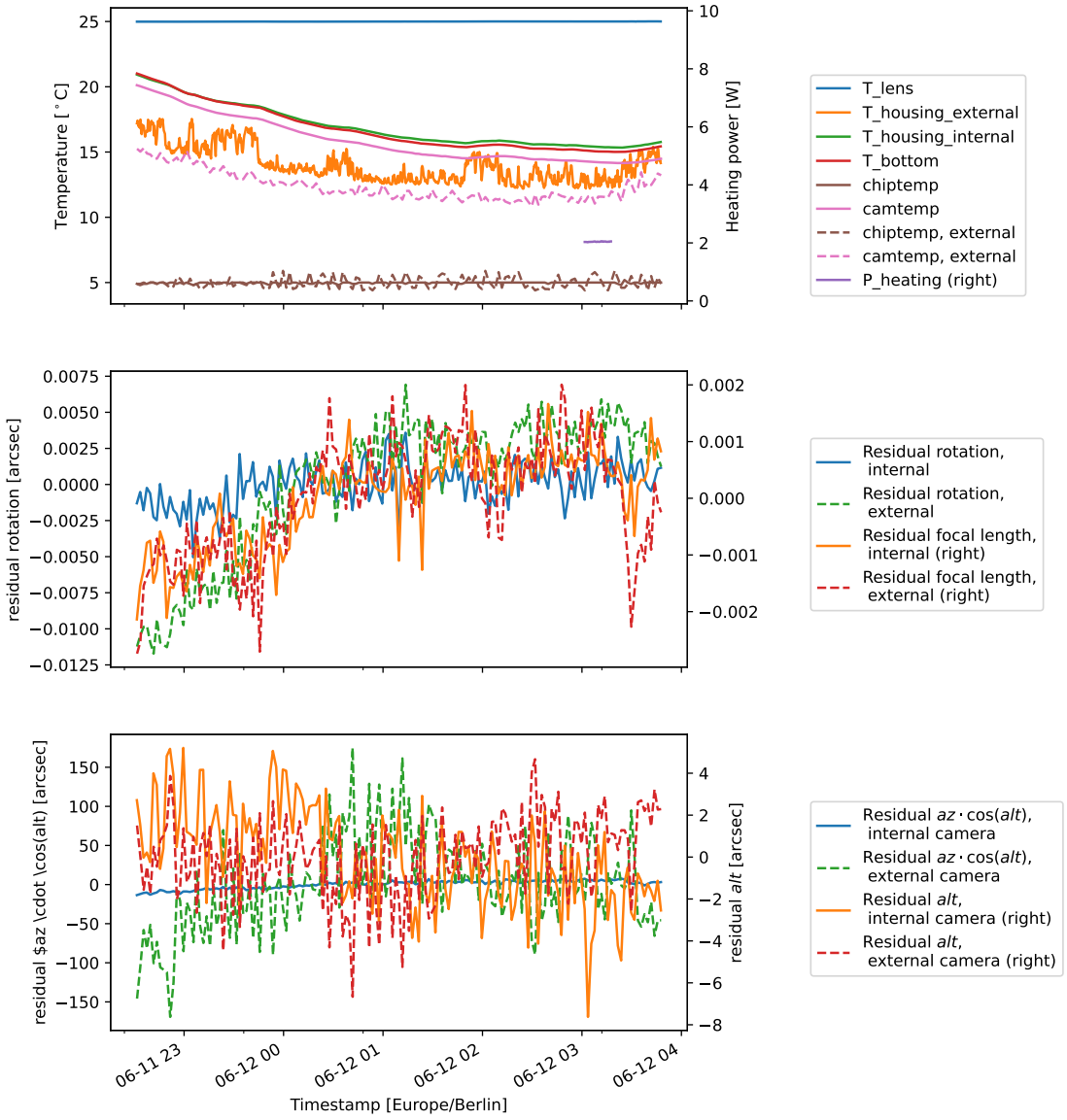

Figure 40: Overview of temperatures and pointing criteria for *Office* campaign.

A.2 Pointing Campaign Overviews

A.2.1 Pointing fits

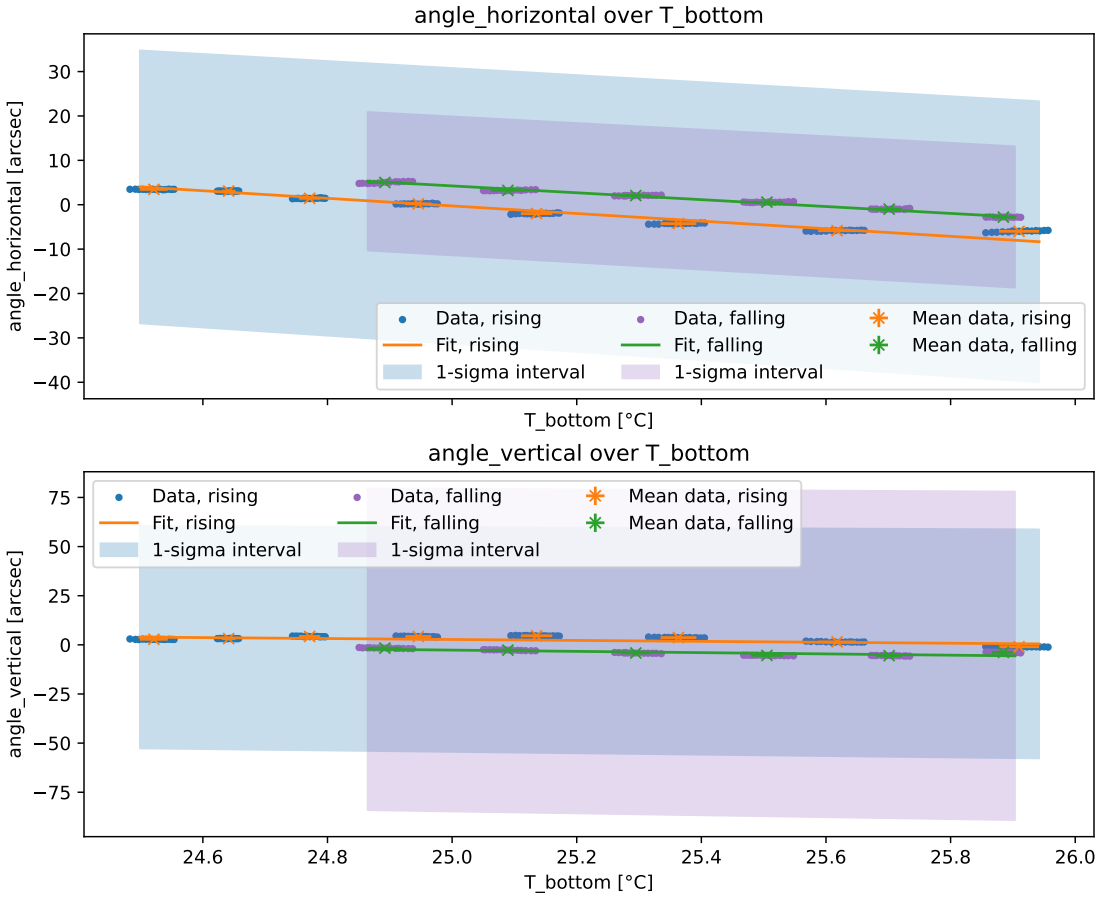

Figure 41: Fit of residual focal length and residual rotation using steadystate-filtered data from lens temperature sweep, using the bottom area temperature as its x axis.

Fit value	Branch	Fit parameters ± fit uncertainty
Residual focal length	↑	$a = (191 \pm 6) \times 10^{-4}\,\mathrm{mm\,K^{-1}}$
		$b = (-480 \pm 13) \times 10^{-3}\,\mathrm{mm}$
	↓	$a = (21.2 \pm 1.1)\,\mathrm{e}-3\,\mathrm{mm/K}$
		$b = (-53.8 \pm 2.6)\,\mathrm{e}-2\,\mathrm{mm}$
Residual rotation	↑	$a = (-1.35 \pm 0.12)\,\mathrm{arcsec/K}$
		$b = (34.1 \pm 2.9)\,\mathrm{arcsec}$
	↓	$a = (-1.04 \pm 0.12)\,\mathrm{arcsec/K}$
		$b = (26 \pm 3)\,\mathrm{arcsec}$

Table 9: Fit parameters for $T = T_{\mathrm{bottom}}$.

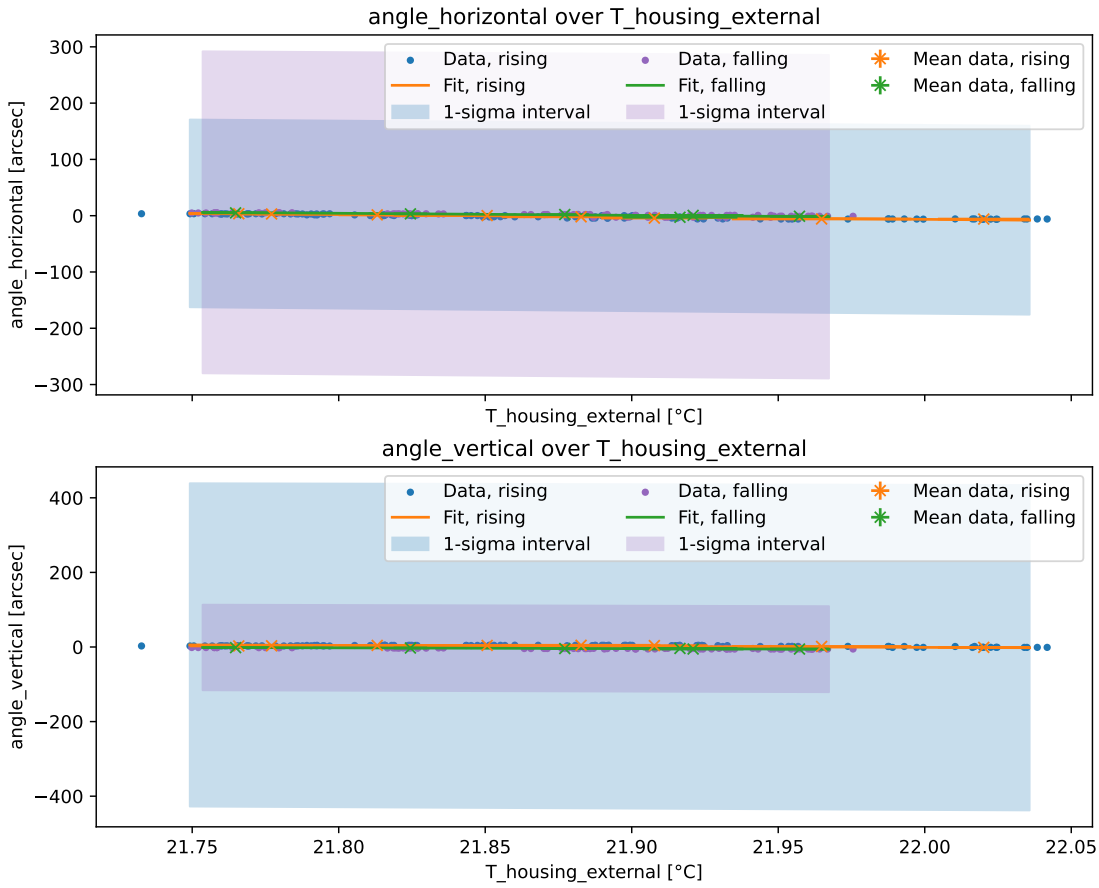

Figure 42: Fit of residual focal length and residual rotation using steadystate-filtered data from lens temperature sweep, using the external temperature as its x axis.

Fit value	Branch	Fit parameters ± fit uncertainty
Residual focal length	↑	$a = (102 \pm 4) \times 10^{-3}\,\mathrm{mm\,K^{-1}}$
		$b = (-224 \pm 8)\,\mathrm{e} - 2\,\mathrm{mm}$
	↓	$a = (101 \pm 20)\,\mathrm{e} - 3\,\mathrm{mm/K}$
		$b = (-2.2 \pm 0.5)\,\mathrm{mm}$
Residual rotation	↑	$a = (-7.3 \pm 0.7)\,\mathrm{arcsec/K}$
		$b = (160 \pm 14)\,\mathrm{arcsec}$
	↓	$a = (-5.1 \pm 2.4)\,\mathrm{arcsec/K}$
		$b = (11 \pm 6) \times 10^{1}\,\mathrm{arcsec}$

Table 10: Fit parameters for $T = T_{\text{housing external}}$.

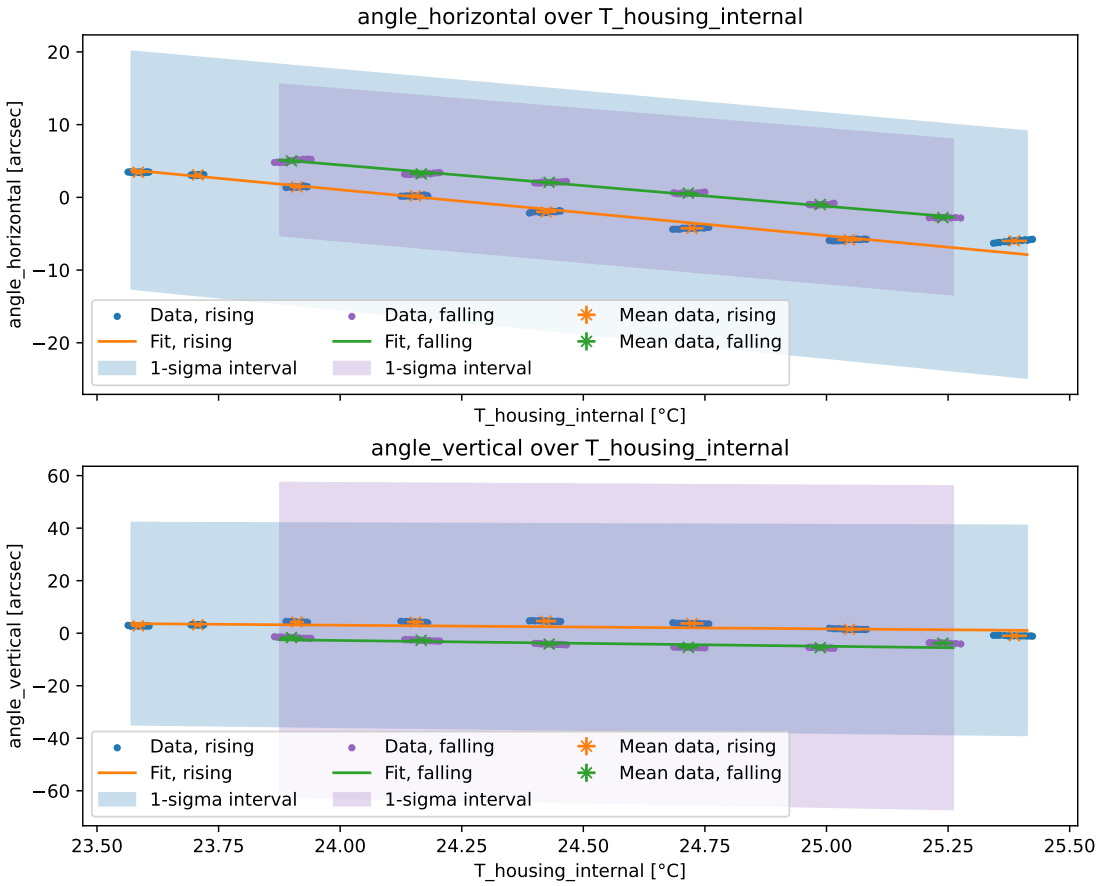

Figure 43: Fit of residual focal length and residual rotation using steadystate-filtered data from lens temperature sweep, using the internal housing temperature as its x axis.

Fit value	Branch	Fit parameters ± fit uncertainty
Residual focal length	↑	$a = (141.5 \pm 2.9) \times 10^{-4}\,\mathrm{mm\,K^{-1}}$
		$b = (-345 \pm 7)\,\mathrm{e-3\,mm}$
	↓	$a = (154 \pm 7) \times 10^{-4}\,\mathrm{mm\,K^{-1}}$
		$b = (-379 \pm 17)\,\mathrm{e-3\,mm}$
Residual rotation	↑	$a = (-1.01 \pm 0.10)\,\mathrm{arcsec/K}$
		$b = (24.9 \pm 2.3)\,\mathrm{arcsec}$
	↓	$a = (-0.77 \pm 0.09)\,\mathrm{arcsec/K}$
		$b = (18.4 \pm 2.1)\,\mathrm{arcsec}$

Table 11: Fit parameters for $T = T_{\text{housing internal}}$.

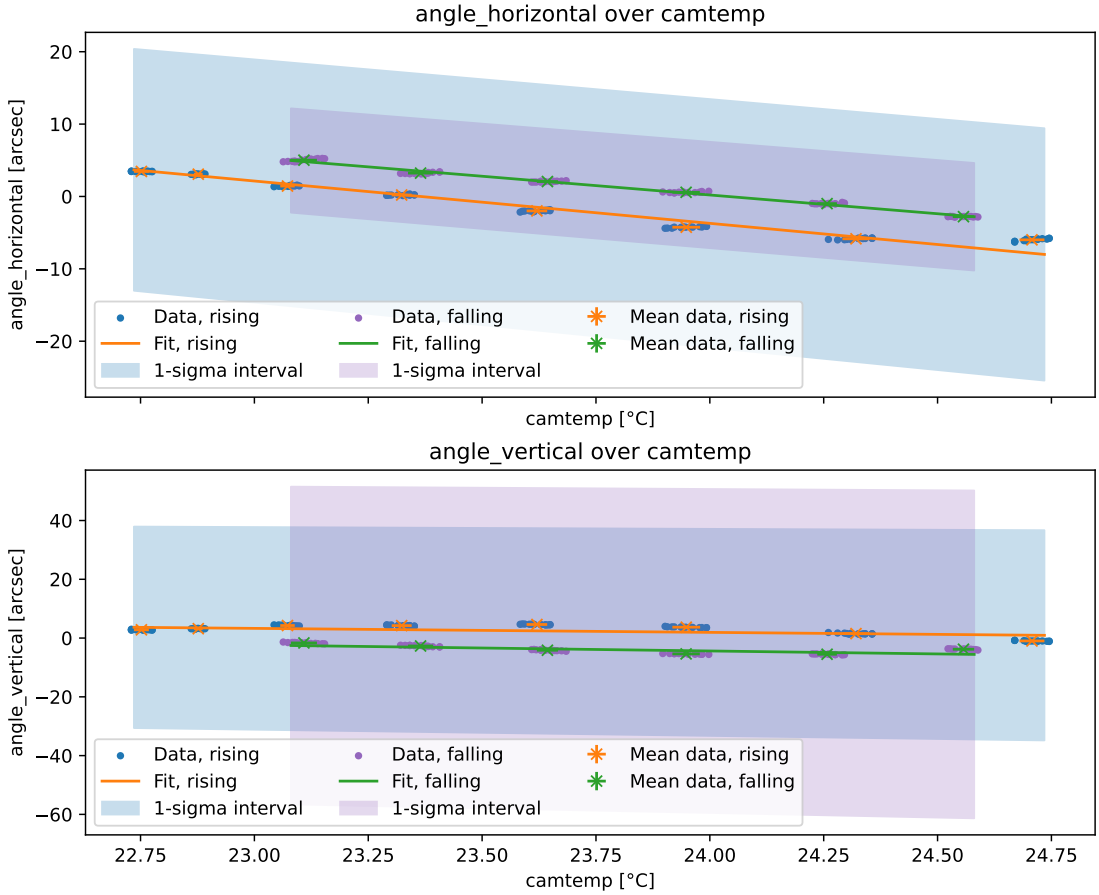

Figure 44: Fit of residual focal length and residual rotation using steadystate-filtered data from lens temperature sweep, using the camera temperature as its x axis.

Fit value	Branch	Fit parameters ± fit uncertainty
Residual focal length	↑	$a = (131.2 \pm 2.1)\,\mathrm{e}-4\,\mathrm{mm/K}$
		$b = (-309 \pm 5)\,\mathrm{e}-3\,\mathrm{mm}$
	↓	$a = (143 \pm 4)\,\mathrm{e}-4\,\mathrm{mm/K}$
		$b = (-339 \pm 10)\,\mathrm{e}-3\,\mathrm{mm}$
Residual rotation	↑	$a = (-0.93 \pm 0.08)\,\mathrm{arcsec/K}$
		$b = (22.2 \pm 1.9)\,\mathrm{arcsec}$
	↓	$a = (-0.70 \pm 0.07)\,\mathrm{arcsec/K}$
		$b = (16.2 \pm 1.7)\,\mathrm{arcsec}$

Table 12: Fit parameters for $T = camtemp$.

A.3 Correlation Analysis

A.3.1 Temperature Sweep

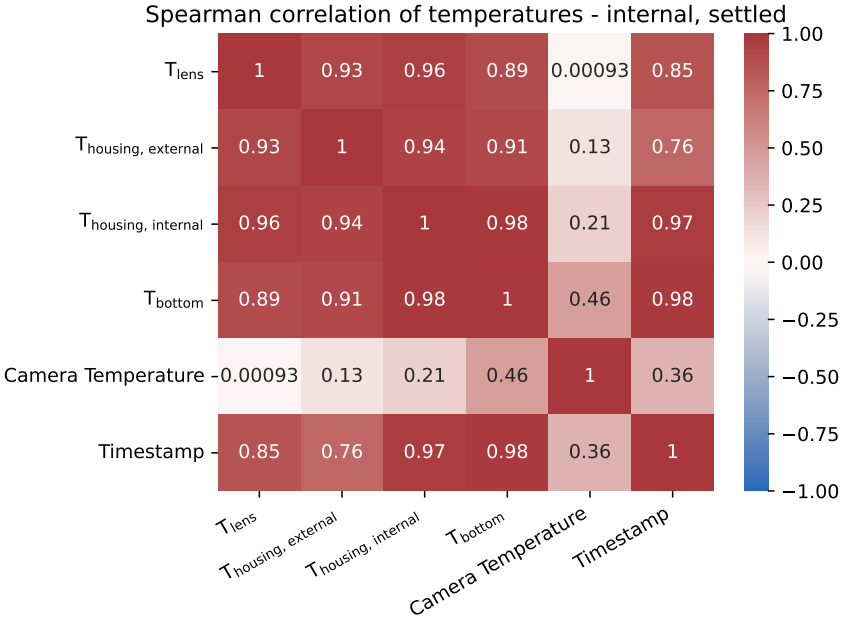

Figure 45: Spearman's rank correlation coefficient of temperature sensors in settled states during laboratory temperature sweep.

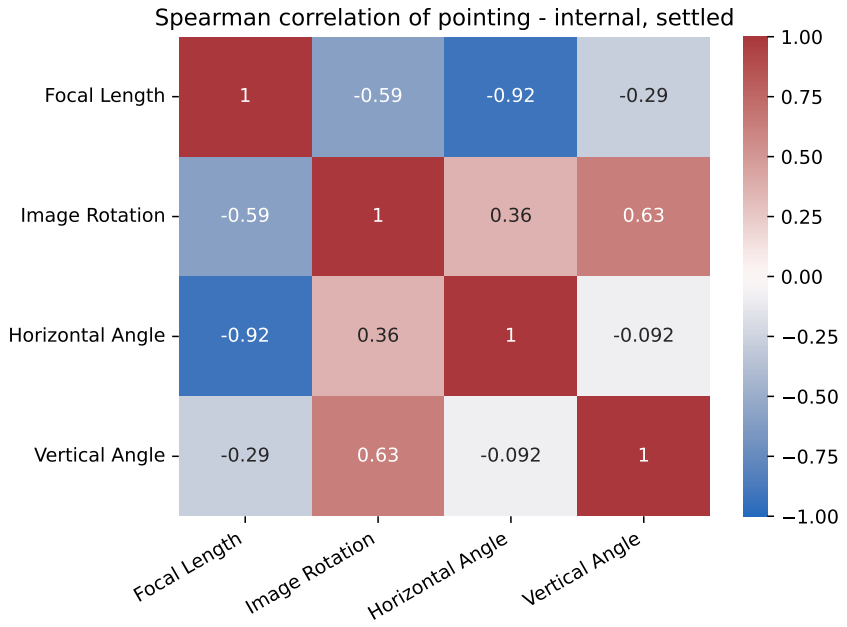

Figure 46: Spearman's rank correlation coefficient of pointing parameters of internal camera in settled states during laboratory temperature sweep.

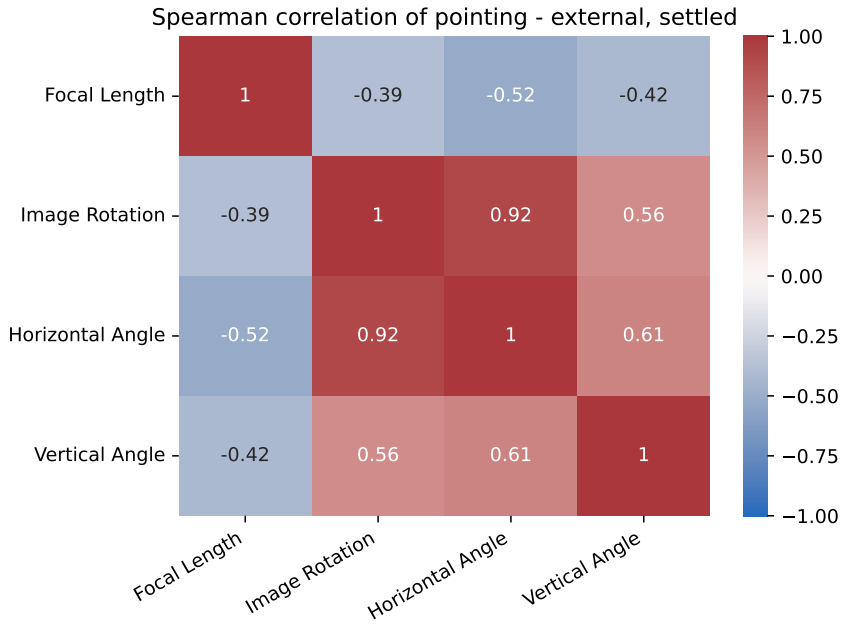

Figure 47: Spearman's rank correlation coefficient of pointing parameters of external camera in settled states during laboratory temperature sweep.

A.3.2 Pointed Campaigns

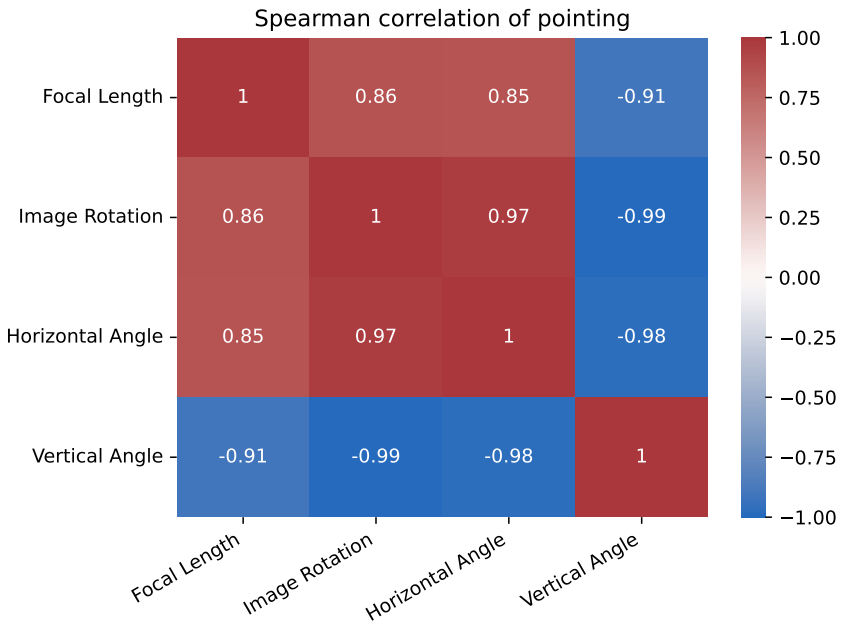

Figure 48: Spearman's rank correlation coefficient of pointing parameters during *Roof 1* campaign.

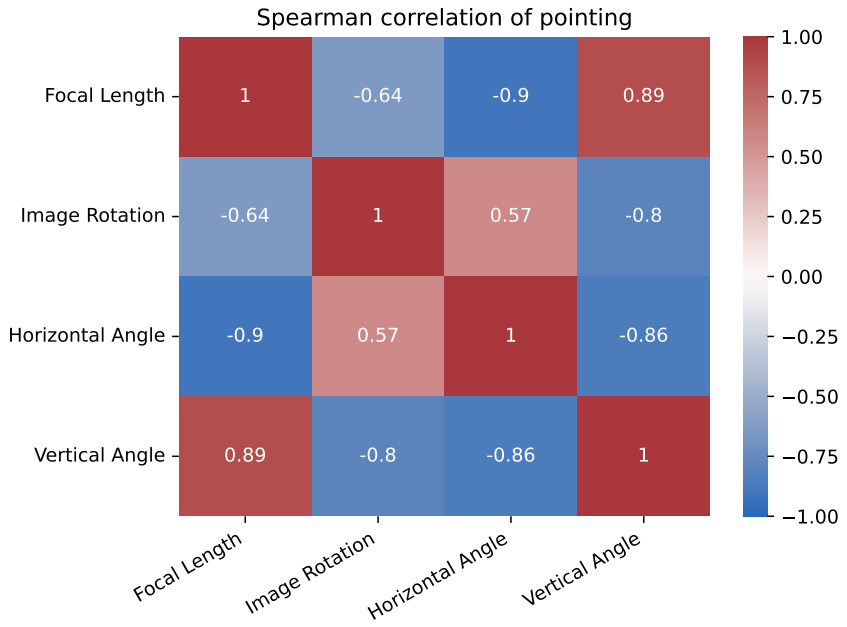

Figure 49: Spearman's rank correlation coefficient of pointing parameters during *Roof 2* campaign.

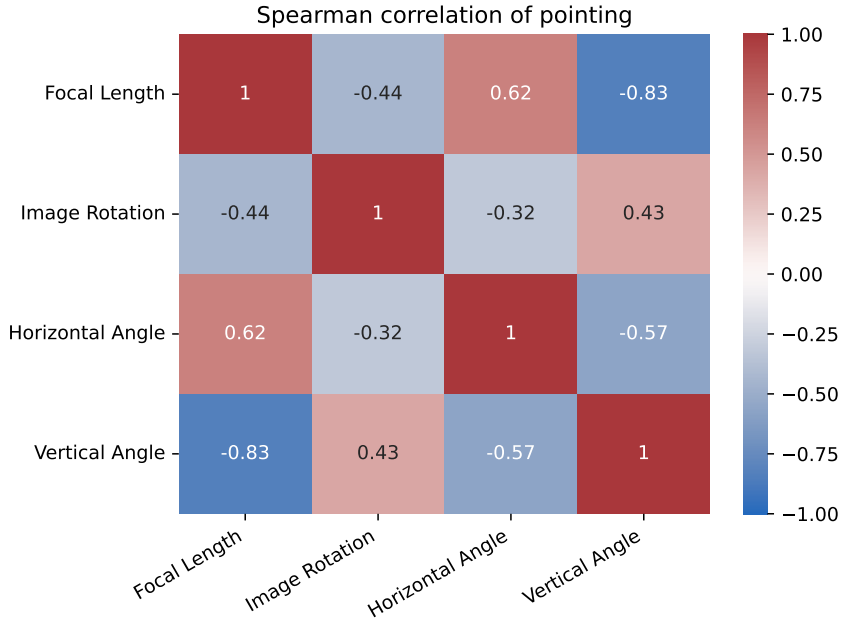

Figure 50: Spearman's rank correlation coefficient of pointing parameters of internal camera during *Office* campaign.

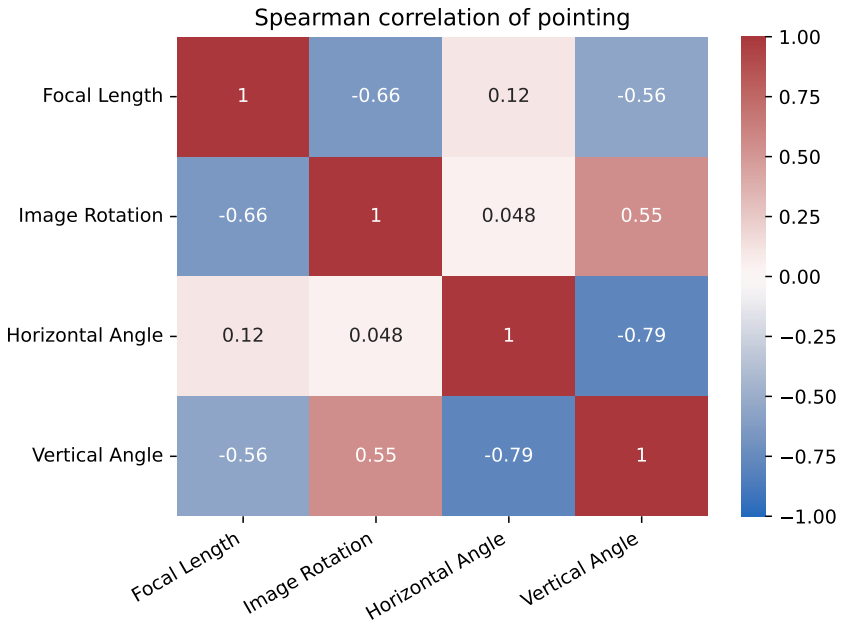

Figure 51: Spearman's rank correlation coefficient of pointing parameters during of external camera *Office* campaign.

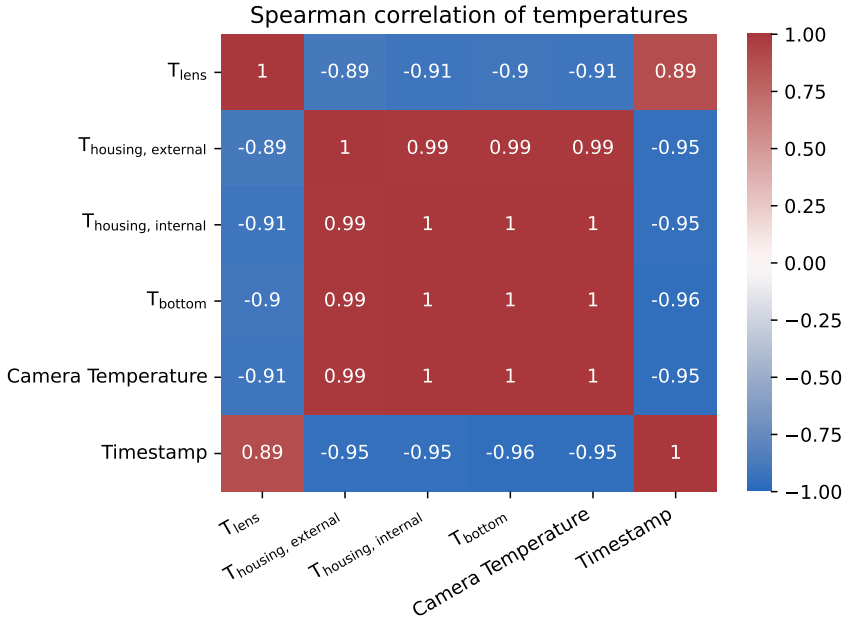

Figure 52: Spearman's rank correlation coefficient of temperature sensors during *Roof 1* campaign.

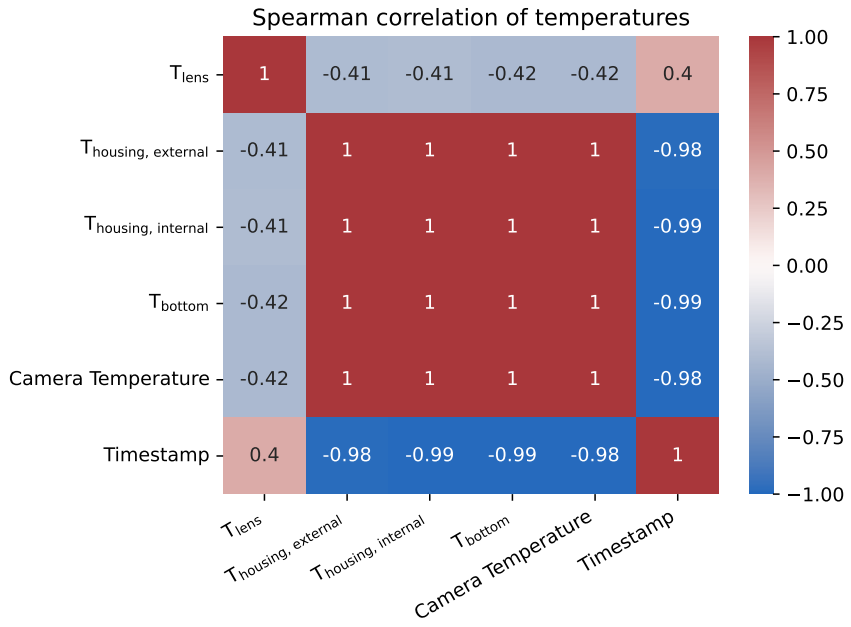

Figure 53: Spearman's rank correlation coefficient of temperature sensors during *Roof 2* campaign.

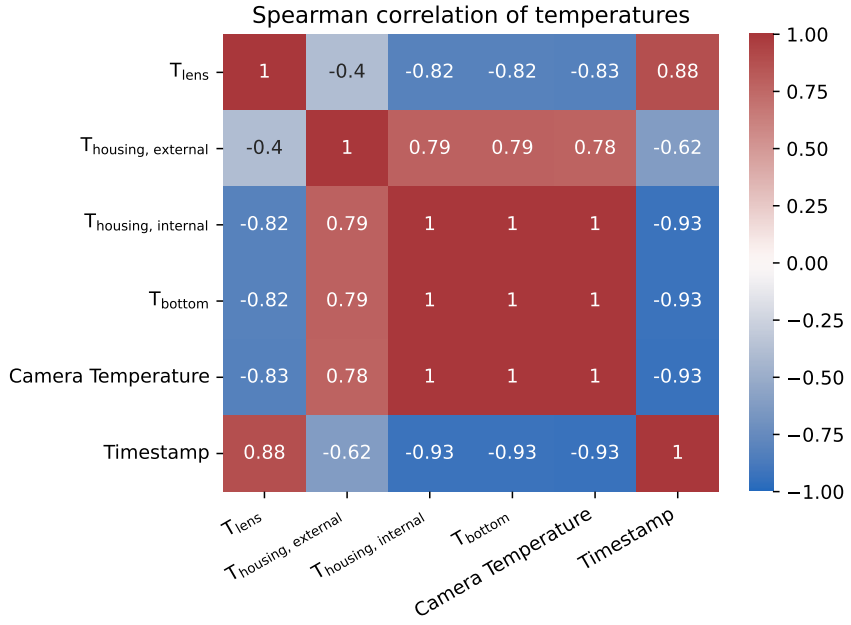

Figure 54: Spearman's rank correlation coefficient of temperature sensors during *Office* campaign.

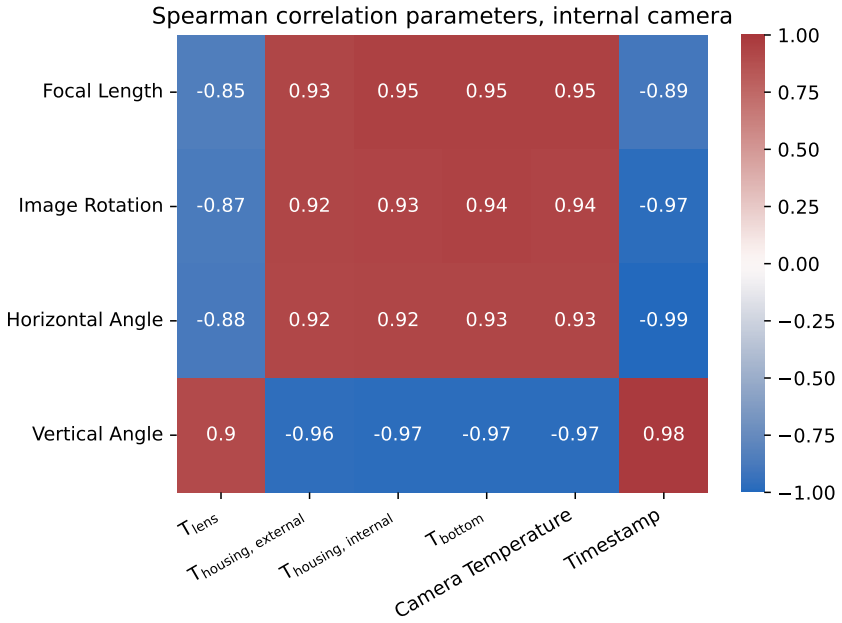

Figure 55: Spearman's rank correlation coefficient of temperatures and pointing parameters during *Roof 1* campaign.

Bibliography

Astrom, Karl Johan and T Hagglund (June 1995). *PID controllers*. 2nd ed. Research Triangle Park: ISA.

Basotect G+ (Oct. 2011). TI G-KT/SM. BASF SE.

Bose, Debanjan, Varsha Chitnis, P. Majumdar, and B. Acharya (Jan. 2022). "Ground-based gamma-ray astronomy: history and development of techniques". In: DOI: 10.48550/arXiv.2201.04719.

Clouds Do Not "Act Like Blankets" (2024). https://www.e-education.psu.edu/meteo3/l2_p10.html. [Online; accessed 02-Aug-2025].

CTAO North - CTAO (2025). https://www.ctao.org/emission-to-discovery/array-sites/ctao-north/. [Online; accessed 09-July-2025].

DIN EN IEC 60751:2023-06 (June 2023).

ESO - Astro Climatology (July 2025). https://www.eso.org/sci/facilities/paranal/astroclimate/climatology.html. [Accessed 09-07-2025].

Fahrmeir, Ludwig, Christian Heumann, Rita Künstler, Iris Pigeot, and Gerhard Tutz (2023). *Statistik*. Berlin, Heidelberg: Springer Berlin Heidelberg.

Garczarczyk, Markus (July 2022). *MST-STR-TDR-36121000-00001 Medium-Sized Telescope Structure Technical Design Report*. Version 2.0.

HAWK, High-Altitude Water Cherenkov Gamma-Ray Observatory (2025). *Detection of cosmic-ray or gamma-ray air showers*. https://www.hawc-observatory.org/science/detection.php. [Online; accessed 03-July-2025].

HESS - The High Energy Stereoscopic System (2021). https://www.mpi-hd.mpg.de/HESS/pages/about/. [Online; accessed 16-July-2025].

Holder, Jamie (2015). *Atmospheric Cherenkov Gamma-ray Telescopes*. arXiv: 1510.05675 [astro-ph.IM]. URL: https://arxiv.org/abs/1510.05675.

Karle, Albrecht (Mar. 2006). *Gamma astronomy with ground based air Cherenkov telescopes and other ground based detectors*. https://user-web.icecube.wisc.edu/~tmontaruli/801/gammaastronomy_karle.pdf. [Lecture; accessed 02-Aug-2025].

Knödlseder, Jürgen (Feb. 2016). "The future of gamma-ray astronomy". In: *Comptes Rendus Physique* 17. DOI: 10.1016/j.crhy.2016.04.008.

Kobzev, Alexander (May 2010). "The mechanism of Vavilov-Cherenkov radiation". In: *Physics of Particles and Nuclei* 41, pp. 452–470. DOI: 10.1134/S1063779610030044.

Konrad Bernlöhr, MPI Heidelberg (2025). *HAWC: the High-Altitude Water Cherenkov Observatory*. https://www.mpi-hd.mpg.de/hfm/CosmicRay/ShowerDetection.html. [Online; accessed 03-July-2025].

Kuhlen, Marco, Vo Hong Minh Phan, and Philipp Mertsch (2023). "Diffusion of relativistic charged particles and field lines in isotropic turbulence". In: arXiv: 2211.05881 [astro-ph.HE]. URL: https://arxiv.org/abs/2211.05881.

MAGIC performance (2025). https://magic.mpp.mpg.de/newcomers/magic-team/technical-implementation0/. [Online; accessed 16-July-2025].

Matzke, Christina (2024). "Design and characterisation of the Pointing LEDs for the Medium-Sized Telescopes of CTA". MA thesis. Erlangen Centre for Astroparticle Physics, Friedrich-Alexander-Universität Erlangen-Nürnberg.

— (2025). personal correspondence.

Observatory, Cherenkov Telescope Array and Cherenkov Telescope Array Consortium (Sept. 2021). *CTAO Instrument Response Functions - prod5 version v0.1*. Version v0.1. Zenodo. DOI: 10.5281/zenodo.5499840. URL: https://doi.org/10.5281/zenodo.5499840.

Power Wirewound Ceramic Resistors, axial (July 2008). KH210-8. Vitrohm.

Prandini, Elisa, Konstantinos Dialektopoulos, and Jelena Strišković (Nov. 2022). "Gamma rays: propagation and detection". In: *Proceedings of Corfu Summer Institute 2021 "School and Workshops on Elementary Particle Physics and Gravity" — PoS(CORFU2021)*. CORFU2021. Sissa Medialab, p. 319. DOI: 10.22323/1.406.0319. URL: http://dx.doi.org/10.22323/1.406.0319.

PT100 Datasheet (2022). [Ord. Nr. 611-7788].

Schaefer, Johannes (2025). personal correspondence.

Schröder, Frank G. (2025). "Radio detection of ultrahigh-energy cosmic-ray air showers". In: *The European Physical Journal Special Topics*. 51.13.04; LK 01. ISSN: 1951-6355, 1951-6401. DOI: 10.1140/epjs/s11734-025-01503-4.

Schwanke, Ullrich, ed. (July 2022). *MST-STR-TDR-36121000-00012 Design and Implementation of the MST Structure Software*. Version 1.0.

Science with the Cherenkov Telescope Array (Feb. 2018). WORLD SCIENTIFIC. ISBN: 9789813270091. DOI: 10.1142/10986. URL: http://dx.doi.org/10.1142/10986.

Specovius, Andreas, ed. (July 2022). *MST-STR-TDR-36121000-00007 MST Pointing Camera: Hardware description*. Version 1.0.

Stanev, Todor (2010). "Cosmic Rays and Extensive Air Showers". In: ed. by Mario Deile, David d'Enterria, and Albert De Roeck.

Steiner, Alexander (June 2022). *MST-STR-ICD-36141000-00005 ICD concerning the MST Pointing Camera and the MST Structure*. Version 1.0.

Technical specifications - CTAO (2025). https://www.ctao.org/for-scientists/technical-specifications/. [Online; accessed 08-July-2025].

Ullrich Schwanke, Christopher van Eldik, ed. (July 2022). *MST-STR-TDR-36121000-00009 Calibration of MST Structures: Mirror Alignment and Telescope Pointing*. Version 1.0.

Welcome to VERITAS (2004). https://veritas.sao.arizona.edu/. [Online; accessed 16-July-2025].

Declaration of Originality

I, Nils Nippe, student registration number: 22953688, hereby confirm that I completed the submitted work independently and without the unauthorized assistance of third parties and without the use of undisclosed and, in particular, unauthorized aids. This work has not been previously submitted in its current form or in a similar form to any other examination authorities and has not been accepted as part of an examination by any other examination authority.

Where the wording has been taken from other people's work or ideas, this has been properly acknowledged and referenced. This also applies to drawings, sketches, diagrams and sources from the Internet.

In particular, I am aware that the use of artificial intelligence is forbidden unless its use an aid has been expressly permitted by the examiner. This applies in particular to chatbots (especially ChatGPT) and such programs in general that can complete the tasks of the examination or parts thereof on my behalf.

Any infringements of the above rules constitute fraud or attempted fraud and shall lead to the examination being graded "fail" ("nicht bestanden").

Place, Date	Signature